Large-Scale, High-Resolution Microelectrode Arrays for Interrogation of Neurons and Networks

Marie Engelene J. Obien and Urs Frey

Abstract High-density microelectrode arrays (HD-MEAs) are increasingly being used for the observation and manipulation of neurons and networks in vitro. Large-scale electrode arrays allow for long-term extracellular recording of the electrical activity from thousands of neurons simultaneously. Beyond population activity, it has also become possible to extract information of single neurons at subcellular level (e.g., the propagation of action potentials along axons). In effect, HD-MEAs have become an electrical imaging platform for label-free extraction of the structure and activation of cells in cultures and tissues. The quality of HD-MEA data depends on the resolution of the electrode array and the signal-to-noise ratio. In this chapter, we begin with an introduction to HD-MEA signals. We provide an overview of the developments on complementary metal-oxide-semiconductor or CMOS-based HD-MEA technology. We also discuss the factors affecting the performance of HD-MEAs and the trending application requirements that drive the efforts for future devices. We conclude with an outlook on the potential of HD-MEAs for advancing basic neuroscience and drug discovery.

Keywords Action potential · Electrical imaging · Electrical stimulation · Extracellular recording · High-density microelectrode arrays

1 Introduction

The next frontier in neuroscience is to map the whole brain and to understand how the networks of neurons within the brain function (Alivisatos et al. 2013; Marblestone et al. 2013). This requires developing techniques for simultaneous

M. E. J. Obien (✉) · U. Frey
Bio Engineering Laboratory, Department of Biosystems Science and Engineering, ETH Zürich, Basel, Switzerland

MaxWell Biosystems, Basel, Switzerland
e-mail: marie.obien@mxwbio.com

recording of neuronal activity at multiple spatial and temporal scales and for manipulating the activity of neurons of interest. At the in vitro level, realizing a high-resolution recording method enables to study neuronal mechanisms and to characterize brain disease models that can be used for drug discovery. Complementary metal-oxide-semiconductor or CMOS-based high-density microelectrode arrays (HD-MEAs) offer a promising platform for high-resolution acquisition of neuronal data. Thousands of neurons can be simultaneously *recorded* and/or electrically stimulated over time scales of microseconds to months. Owing to the high-density feature, a single neuron can be recorded by hundreds of electrodes. This facilitates assigning recorded spikes to their source neurons, termed *spike-sorting*, and allows for the subcellular mapping of a neuron's axonal arbor.

Electrical recording of neuronal activity has been popularly used for analyzing single neurons and neuronal networks (Contreras 2004; Llinas 1988). Electrical signals produced by neurons can be detected at a distance from the source. Several recording tools apply to different spatial scales. At the mesoscale, where local neuronal populations can be analyzed, a popular method is extracellular recording using metal electrodes. An electrode placed inside a brain slice in vitro or inserted in the brain in vivo detects electrical signals produced by the surrounding cells. A wide range of neural phenomena can be observed, from the spiking activity of individual neurons (extracellular action potentials or EAPs; bandwidth: 300–3000 Hz) to the slower network activity of small populations (local field potentials or LFPs; bandwidth: 1–300 Hz), shown in Fig. 1. Additionally, the same electrode can be used to deliver electrical stimulation to a local area in the brain. While this method for brain recording and stimulation is relatively easy, the challenge lies in making sense of the recorded data. With hundreds of possible signal sources surrounding an electrode, the specificity and selectivity of such technique is poor. Thus, *extracellular recording* has been widely used for analyzing population activity. In contrast, *intracellular recording* by patch clamp has been the gold standard for analyzing single neurons and synaptic connectivity of a few cells. However, patch

Fig. 1 Extracellular and intracellular recording. Left: Illustration of cells across cortical layers modified with permission from Buzsáki et al. (2012). Right: Signals of simultaneous extracellular recording and intracellular whole-cell patch-clamp recording modified with permission from Henze et al. (2000)
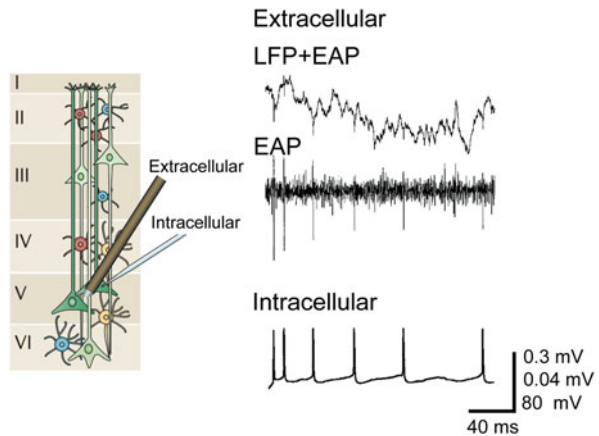
clamp necessitates intricate skill to perform. The viability of patched neurons lasts only up to a few hours. Moreover, current implementations of the experimental setup are bulky. All these limit the capability of the patch-clamp technique to scale for studying networks of neurons (Wood et al. 2004).

To achieve high-resolution activity mapping of neuronal networks, multiple electrical sensors tightly spaced in an array can be utilized. Microelectrode arrays (MEAs, also termed multielectrode arrays) allow for simultaneous long-term recording of LFPs and EAPs from a population of neurons at submillisecond time scale. In order to increase spatial resolution, that is, to place thousands of electrodes per square millimeter, the area taken up by wiring between electrodes-to-readout circuitry has to be reduced. This has been made possible by using industrial CMOS technology to create high-density MEAs (HD-MEAs). As an added benefit, readout circuitry, such as amplifiers and analog-to-digital converters, can be included on the same substrate as the electrodes in order to improve signal quality. The design of the on-chip signal conditioning circuitry should consider the electrode impedance and the possible sources of noise to ensure high quality signals. HD-MEAs with good signal-to-noise ratio (SNR) can be used to map single neuronal activity at subcellular resolution and to observe network activity at the same time (Ballini et al. 2014; Dragas et al. 2017; Frey et al. 2010), illustrated in Fig. 2.

1.1   Terminology

Over the years, a wide repertoire of terms has been used to refer to and distinguish between all the different forms of MEAs, for example emphasizing the type of transducers used (multitransistor array, microelectrode array, multielectrode array, micronail array, capacitive-coupled array, 3D MEA), the type of substrate (active array, passive array, silicon array, CMOS array), the shape of the device (needle-type probe, polytrode, neuro dish), the channel count (multichannel array), the electrode density (HD-MEA) or the application (implantable array, in vivo MEA, in vitro MEA), and more. We would therefore like to briefly explain the terminology used in the context of this chapter.

We generalize the term MEA to cover both substrate-integrated planar MEAs and implantable neural probes. We also include capacitive-coupled devices, such as multitransistor arrays in the definition of MEAs. We then distinguish between implantable, in vivo MEAs, such as polytrodes and neural probes, and in vitro MEAs that generally include a cell culture dish or other types of medium chamber. We use the term "array" to refer to the actual area that encompasses the transducer elements only, and we use device or MEA to refer to the entire device. With system, we refer to the MEA and all required components to operate it, such as the data acquisition hardware and software. We use the terms "active" and "passive" to distinguish between devices with active circuit elements, such as transistors, and devices without such elements.
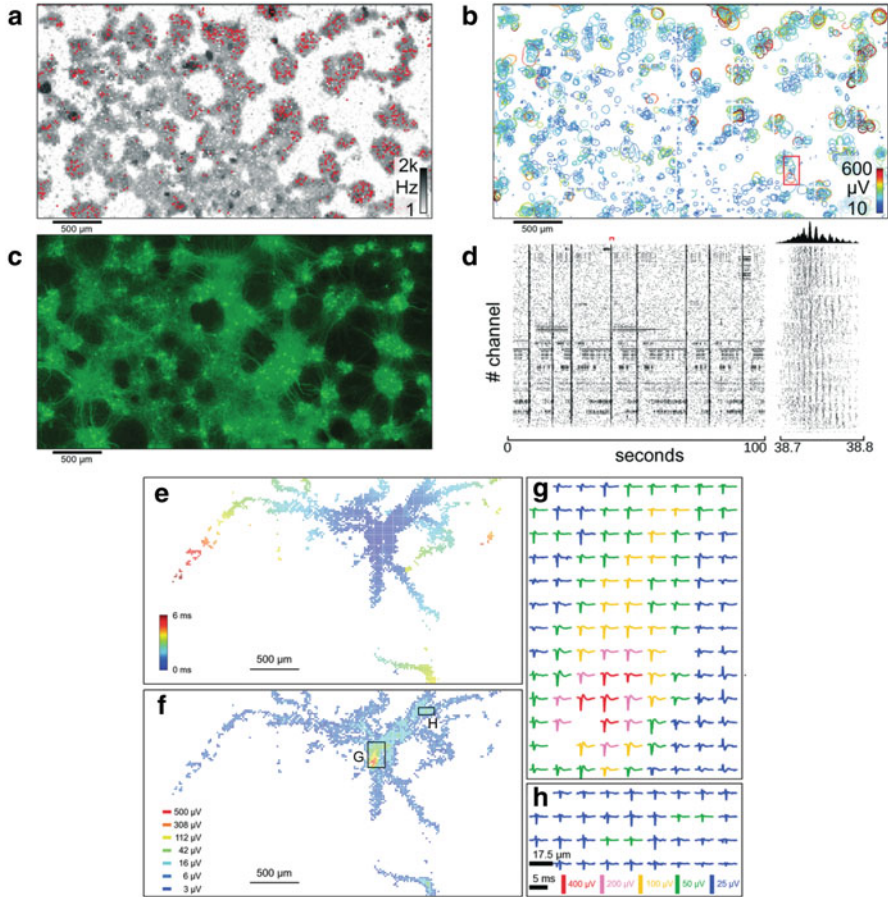
Fig. 2 Obtaining network-wide and single-neuron activity maps using CMOS-based HD-MEAs. (A-D) Networks. (**a**) Average EAP firing rate as measured by each electrode (26,400 electrodes in total) shown as pixels colored with a logarithmic gray-scale between 1 and 2 kHz. Red dots correspond to the electrodes selected for the raster plot in (**d**). (**b**) Representation of all 2000 individual neurons identified through spike-sorting the signals. A circle represents each detectable cell; the edges indicate where the amplitude of the measured signals exceeds −4.5 standard deviations of the electrode noise. The colors correspond to the amplitude of the most negative peak detected by the electrodes within the circle. (**c**) Fluorescence image of transfected cells (around 5% of all cells in the culture). (**d**) Raster plot of 100 s of activity for 1024 electrodes recorded simultaneously. Red marker shows the time period in close up view (bursting activity) on the right. Histogram at the upper right shows the number of spikes per time bin of the burst close up. (**e–h**) Single neuron electrical footprint. (**e**) All electrodes that captured activity attributed to a single neuron are colored according to the time of arrival of the AP at the electrode locations. (**f**) The same electrodes in (**e**) are colored according to the amplitude of the most negative peak detected. (**g–h**) Spike-triggered averages (30–50 averages) of the EAP electrical footprint from the two areas of the array as indicated by black boxes in (**f**). All figures modified with permission from Müller et al. (2015)

2 CMOS-Based HD-MEA Technology

Since the single extracellular microelectrodes used in the middle of the last century (Gesteland et al. 1959; Weale 1951), development quickly proceeded to MEAs with multiple transducers for the purpose of increasing the number of neurons observed (Csicsvari et al. 2003; Gross et al. 1977; Pine 1980; Thomas et al. 1972) and to increase reliability of spike sorting (Gray et al. 1918; Harris et al. 2000). Passive transducer devices based on electrodes embedded in glass or silicon substrates with fixed wiring to amplifiers for in vitro and also in vivo applications became commercially available in the late 90s and early years of this century.

A wave of fabrication and semiconductor technological advances paved the way towards the miniaturization of modern biosensor devices. Microelectrode arrays have thus been improved by integrating active electronic components in the same substrate, together with the electrodes. A technology for constructing integrated circuits is called complementary metal-oxide-semiconductor (CMOS), hence the term CMOS-based MEAs. Already early on, silicon-based biosensors for interfacing cells with microelectronics were developed (Bergveld 1970; Parce et al. 1989). Active devices, employing FETs were fabricated and 2D arrays demonstrated (Besl and Fromherz 2002). Devices using CMOS technology were fabricated in academic facilities (DeBusschere and Kovacs 2001) and industrial foundries, usually in conjunction with additional processing steps for biocompatibility reasons (Berdondini et al. 2002; Eversmann et al. 2003; Franks et al. 2003). Later on, similar to CMOS cameras, MEAs have been developed with thousands of electrodes, producing high-density microelectrode arrays (HD-MEAs) while also improving the signal quality of recordings (Hierlemann et al. 2011; Obien et al. 2015). Tapping into the large and established CMOS production industry provides an economy of scale for HD-MEA production.

The key advantage of integrating active electronic components on the same substrate as the actual electrodes is the possibility of a much higher electrode number and density. Due to the possibility of using active switches to time multiplex signals, integrated circuits make it feasible to transfer data from such high channel counts off chip and to overcome the connectivity limitation of passive devices. Additionally, such cointegration allows for amplifying the signals with optimal quality, due to minimal parasitic capacitances and resistances (Hierlemann et al. 2011). The monolithic cointegration also allows for including additional functionality, for example, on-chip spike detection, closed-loop capabilities, electrical stimulation, electronic chip identification, device calibration, and other types of sensing modalities, such as temperature, pH, and optical or neurotransmitter sensing (Baumann et al. 1999; Dragas et al. 2017; Johnson et al. 2013b; Park et al. 2017; Tokuda et al. 2006).

2.1 MEA Types

MEA architectures have evolved throughout the years. In general, the electrode-to-readout routing scheme can be divided into two types: fixed wiring, that is, each electrode is directly wired to outside of the array, connecting to the signal conditioning circuit; and multiplexed array, that is, routing from electrodes traverses switches before reaching the signal conditioning circuit. We further classify the MEA device types, shown in Fig. 3.

Passive Conventional MEAs have fixed wiring and are passive (i.e., no active circuit elements, such as amplifiers). Each electrode connects directly to a signal pad outside the array through a wire. The pads are then connected to external equipment for signal conditioning. Passive MEAs are typically easier to fabricate and many different substrates and electrode materials can be used. The user has direct access to all electrodes simultaneously, however, wiring and electrode geometry limit the total number of electrodes that can fit in a given area. Examples of passive MEAs
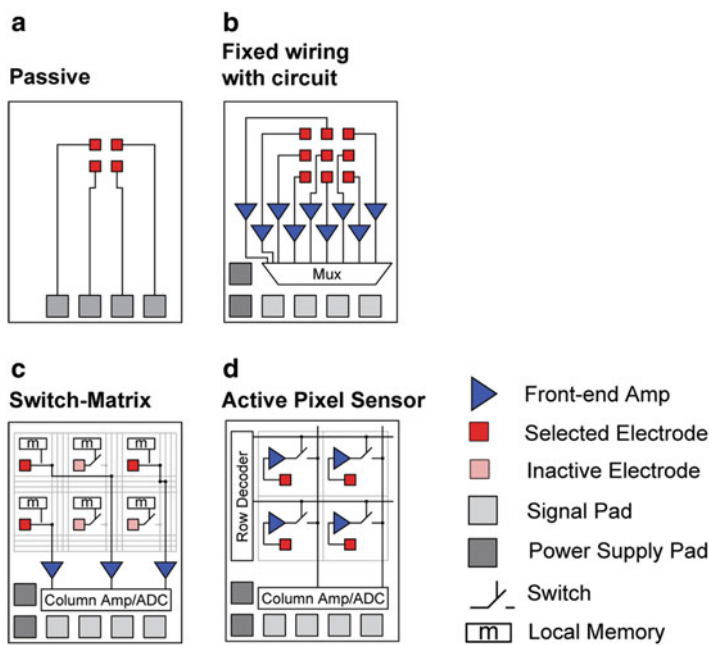
Fig. 3 MEA architectures. This table summarizes the different architectures used for MEAs. (**a**) Passive: Fixed wiring with electrodes directly connected to signal pads and no active circuitry. (**b**) Fixed wiring with electrodes directly connected to on-chip active circuitry for signal conditioning. (**c**) Switch-matrix (SM): Multiplexed array with flexible addressing achieved by adding more routing resources within the array. (**d**) Active pixel sensor (APS): Multiplexed array with all electrodes sampled at fast speeds for a full-frame readout. Modified with permission from (Obien et al. 2015)

were developed and used by Alpha MED n.d., Multi Channel Systems GmbH n.d., Greschner et al. (2014), Gross et al. (1977), Litke et al. (2004), Nisch et al. (1994), Oka et al. (1999), Pine (1980), Regehr et al. (1989), Segev et al. (2004), and Thomas et al. (1972).

Fixed Wiring with On-Chip Circuitry These types of MEAs have electrodes directly wired to on-chip active circuit elements that are used for signal conditioning, such as amplification and filtering. One variation employs multiplexers to allow readout of more electrodes despite a limited number of signal output pads. Multiplexing can be done only if the amplifiers and filters are before the multiplexer. Although this architecture allows for increased electrode count, the electrode density cannot be maximized (i.e., direct wiring of each electrode to signal conditioning circuitry limits how close electrodes can be packed together). Selected fixed wiring with on-chip circuitry MEA references are (DeBusschere and Kovacs 2001; Greve et al. 2007; Offenhäusser et al. 1997).

For in vivo MEAs, the connectivity limitation is even more severe, as connections cannot be wired out on all four sides of the array, but only on one of the narrow sides. Examples of in vivo passive and fixed wiring devices are (Berényi et al. 2014; Blanche et al. 2005; Csicsvari et al. 2003; Du et al. 2011; Fujisawa et al. 2008; Gray et al. 1918; Herwik et al. 2009; Jones et al. 1992; Kipke et al. 2003; Montgomery et al. 2008; O'Keefe and Recce 1993; Olsson and Wise 2005; Wise et al. 1970)

Switch-Matrix (SM) The switch-matrix (SM) concept uses transistors to implement switches within the array to route signals from electrodes to readout circuitry placed outside the actual electrode array.

In the SM concept, these routing means is operated in static mode, meaning that some electrodes are selected by opening or closing the switches and a recording is then started without changing the electrode selection. Typically, not all electrodes detect activity during an MEA experiment, thus choosing a subset of "interesting" electrodes is possible. A common protocol is to first scan all the electrodes in successive recordings to determine which electrodes to later continuously record during an experiment. The advantage of this concept is that large, low-noise amplifiers can be implemented outside the actual electrode array, allowing to optimize amplifiers for best possible SNR. SM MEAs have been implemented and various degree of flexibility that the routing means provide. Very simply row, column-based selectability has been implemented (Huys et al. 2012). Increased degree of freedom in selecting subsets of electrodes was achieved for the following in vivo probes (Lopez et al. 2014, 2016, 2018; Seidl et al. 2011). The availability of a large set of wires, switches, and local memory allows for even more complex routing paths that connect a subset of electrodes to the readout and stimulation channels in a flexible manner. Frey et al. (2010) use 1.2 memory cells on average per electrode, allowing already fairly complex routing. Ballini et al. (2014) use 2.2 memory cells per electrode, drastically increasing the possibilities in selecting subsets. Viswam et al. (2016) increased the number of bits per electrode to more then 3, virtually allowing arbitrarily subset selections. Switch-matrix MEAs were

developed by Ballini et al. (2014), Dragas et al. (2017), Frey et al. (2010), Huys et al. (2012), Lopez et al. (2014, 2016, 2018), Seidl et al. (2011) and Yuan et al. (2018).

Full-Frame Readout (Active Pixel Sensor or APS) Similar to image sensors used in cameras, all electrodes in active pixel sensor (APS) MEAs can be sampled at fast speeds in full-frame readout. Typically, rectangular subarrays can be chosen as regions of interest and sampled at faster rates than full-frame readout. For full-frame readout, the front-end amplification and filtering have to be before the multiplexing, meaning that the front-end amplifier has to be located within the pixel itself. This is because the electrode exhibits high impedance and therefore, without an amplifier, cannot drive multiplexed readout lines at sufficient speed. The small pixel area (i.e., available area near each electrode) serves as a limitation to designing very low noise circuitry for APS MEAs, since small-sized amplifiers inherently generate larger noise levels. Thus, while all electrodes can be recorded at the same time, only relatively large signals are detectable from noise. Examples of APS MEAs are Angotzi (2018), Aziz et al. (2009), Berdondini et al. (2009), Bertotti et al. (2014), Eversmann et al. (2003, 2011), Heer et al. (2006), Johnson et al. (2013a, b), Maccione et al. (2013), Ogi (2017), Park et al. (2017), Shahrokhi et al. (2009), Tsai et al. (2017), and Yuan et al. (2018).

2.2 Developments in MEA Technology

The evolution of MEAs with respect to overall sensing area and electrode densities is illustrated in Fig. 4a. A variety of historical and current MEA devices are included. The electrode count is shown with solid lines. The devices are categorized into "passive" (including both passive and fixed wiring MEAs) and "active" (multiplexed arrays such as SM and APS HD-MEAs). Recent HD-MEAs (SM and APS) aim to increase the total number of electrodes and the spatial resolution to allow for ever more demanding applications to be executed. One parameter used to characterize the density of MEAs is *single-cell separability*. Here, we used a threshold of 1000 electrodes per mm^2 as the minimum requirement to effectively assign spikes to a neuron.

The design of on-chip signal conditioning is crucial to achieve high quality signals. However, due to area availability and power consumption limitations, there remains a compromise between the quality of recorded signals and the number of parallel electrodes readout. SM HD-MEAs prioritize signal quality, while APS HD-MEAs target a high number of parallel readout channels, see Fig. 4b. We consider 10 μVrms as the minimum noise requirement for effective *spike detectability*. Figure 4b illustrates the tradeoff between the number of parallel (or quasi parallel) readout channels and the total input referred noise of the amplification chain. It shows the fundamental fact that a low-noise front-end amplifier requires both area and power. Limiting either will inherently increase the noise levels. The power
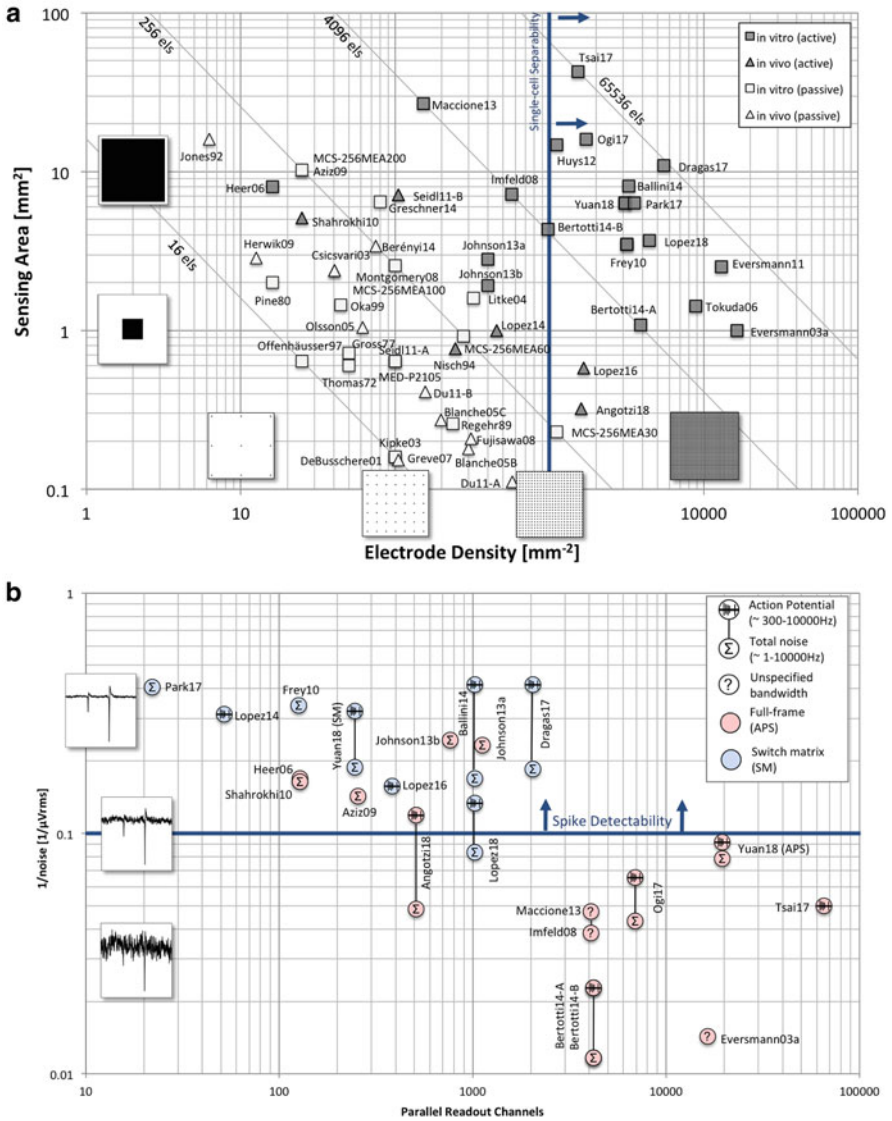
Fig. 4 Device comparison. (**a**) HD-MEA in vivo and in vitro implementations are shown according to the sensing area size and electrode density. For devices with a regular sensor pitch, such as most in vitro MEA devices, the total area is calculated as number of electrodes times the pixel area. For all devices, the number of electrode times the inverse of the electrode density matches the total area. The light gray lines illustrate the number of electrodes. (**b**) CMOS-based MEAs are compared with respect to parallel recording channel count and noise level. The noise values shown are approximated root-mean-square values stated in the respective citations. Note that the conditions under which these measurements were taken usually differ significantly (noise bandwidth, inclusion or exclusion of electrode noise, inclusion of ADC quantization noise, etc.). This graph only serves as a rough comparison, indicating noise values under both known and unknown conditions. The waveforms to illustrate the noise levels are simulated and have a spectrum

budget for the entire device, including all circuitry within the array and surrounding it, is limited by the amount of produced heat that one can tolerate. For the area constraints, one has to separately consider the area within the array and surrounding it. Within the array, the electrode density dictates the available area per pixel. Outside the array, the area is limited mostly by the fabrication cost.

2.2.1 Electrodes and Transducers

Choosing the materials for the insulator, conductor, microelectrode, and substrate is crucial, in particular with respect to biocompatibility. Various techniques for fabricating microelectrodes have been reviewed in Huang et al. (2009), Li et al. (2003), and Park and Shuler (2003). All materials that will be in contact with or near cells and tissue need to be tested for toxicity in prolonged periods of time (Hassler et al. 2011). It is also important to consider the biological experiments for which the microelectrodes will be used, whether in vivo or in vitro, chronic or acute recording. Moreover, deciding the type of MEA to use is highly dependent on the type of recorded signals needed, whether EAPs and/or LFPs or intracellular action potentials (IAPs), single cell resolution or not. If the MEA is to be used for stimulation, the charge capacity of electrodes is an important aspect. The electrode needs to be able to mediate reactions at the electrode–electrolyte interface to allow electron flow in the electrode to transition into ion flow in the electrolyte towards stimulating nearby cells (Cogan 2008).

Generally, an important goal of electrode fabrication is to achieve low impedance. Low electrode impedance results in higher signal-to-noise ratio (SNR), with a typical target SNR of 5:1 or higher (Cogan 2008). Oppositely, high electrode impedance combined with a large parasitic capacitance and amplifier input capacitance (see Sect. 2.3) will negatively affect recordings, especially at higher frequencies (Cogan 2008; Robinson 1968). In addition, uniformity of the electrode impedance across an array of electrodes may be important to obtain consistent data.

Typically, electrodes are made with metallic conductors such as gold (Au), titanium nitride (TiN), platinum (Pt), stainless steel, aluminum (Al), and alloys like iridium oxide (IrOx). Since the electrodes used in MEAs are on the micrometer scale, it is a challenge to achieve low electrode impedance with plain conductors only. Increasing the effective surface area of electrodes can be achieved by modification with porous conductive materials such as Pt-black, Au nanostructures, carbon nanotubes (CNTs), TiN, and conductive polymers like poly(3,4-

---

Fig. 4 (continued) typical for MEA recordings. The simulated spikes in the boxes (left) are typical spikes for acute brain slice measurements recorded with microelectrodes. The recorded amplitudes may vary significantly depending on preparation and sensor characteristics. Modified with permission from Obien et al. (2015)

ethylenedioxythiophene) (PEDOT). Emerging materials aside from PEDOT and CNTs include doped diamond and graphene. By modifying the surface, the electrode impedance can be decreased drastically and neuronal recording can be improved (Cui et al. 2001; Franks et al. 2005; Keefer et al. 2008; Ludwig et al. 2006; Viswam et al. 2014). See Kim et al. (2014) and Nam and Wheeler (2011) for a review of electrode materials and surface modification.

Nonmetallic electrodes have been mostly used in conjunction with field-effect transistor (FET)-based transducers (Bergveld 1970; Fromherz et al. 1991). An OGFET can, for example, be obtained if the fabrication process of an FET is stopped before depositing the gate material (Jenkner et al. 2004). Easier to fabricate is the so-called extended-gate FET (EGFET), in which the FET is fabricated without modification from a standard CMOS process. Metal and via interconnections are used to extend the gate to the surface of the chip, where an insulated electrode implements the "extended gate." Such insulation ensures that no faradaic currents occur. However, as Hierlemann et al. pointed out, devices with metal electrodes also usually connect to an FET directly (Imfeld et al. 2008) or through a filter capacitor (Heer et al. 2006), resulting in a largely capacitive recording situation (Hierlemann et al. 2011). OGFET, EGFET, and devices that directly connect the electrode to the first FET usually need to include some measures to properly bias the gate or some calibration mechanism, which may cause transient currents to flow at the electrode. Whereas for devices with a capacitively coupled front-end stage, controlling the electrode input node is generally not needed. Devices with an FET-based transducer, but using a metalized gate exposed to the liquid, have also been developed (Jobling et al. 1981).

Recently, ultrasmall electrodes are being developed to record intracellular activity, including subthreshold signals, as reviewed in (Spira and Hai 2013). This is achieved by 3D structured electrodes such as silicon nanowires (Robinson et al. 2013), plasmonic antennas (Dipalo et al. 2018), and Au mushrooms (Hai et al. 2009) penetrating the cell membrane. Electroporation was shown to facilitate measurement of intracellular activity (Hai and Spira 2012; Koester et al. 2010).

2.2.2 MEA Recording Hardware

Apart from the electrode array, CMOS devices also require the design of neuronal amplifiers and some sort of data transmitter, either of the amplified analog signals or, more typically, of the already digitized data. Generally, a neural amplifier needs to have high input impedance, which is significantly higher than the electrode impedance, to ensure signal integrity. The amplifier should be of low power to prevent substrate heating that could damage cells or tissue. For in vitro MEA devices, a variety of target applications have to be considered. Therefore, gain and dynamic range requirements can be quite demanding and should be adjustable, such as to cover applications with maximal amplitudes of a few hundred microvolts in acute slice preparations and, on the other hand, up to 10 mV in measurements from cardiomyocytes. The same also holds true for the flexibility in the recording

bandwidth. Some applications may require either lower frequency signals or spikes in the EAP band only, while some experiments target both bands with different gain requirements at the same time. The circuits need to implement some sort of high-pass filter to block the large *1/f* noise of the electrode–liquid interface typically observed.

MEA systems can also include digital-to-analog conversion (DAC) and stimulation circuitry (discussed in the next subsection). MEA systems need to include an interface to transmit the data and receive commands for controlling the system's operation. The requirements are different for implantable devices, where usually the target application is much more defined, but also the power, reliability, and safety requirements are more stringent. These systems often implement spike detection or classification and wireless transmission in the system, either as a monolithic implementation or hybrid approach using multiple ICs. They may also be powered wirelessly. On the other hand, in vitro MEA systems do not require wireless power or data transmission, as they can generally be directly wired to the data-receiving device. In this case, often common interface standards are employed, such as USB (Multi Channel Systems GmbH), Ethernet (Frey et al. 2010), National Instrument's DAQ card (Alpha MED n.d.), CameraLink (Imfeld et al. 2008), or others. Most of these systems support online storage of the full raw data to hard disks, sometimes including some form of lossless data compression (Sedivy et al. 2007).

2.2.3 Electrical Stimulation

MEAs allow observation of neural activity, but can also influence and control activity. Metal electrodes can deliver electrical stimuli directly. CMOS fabrication allows including electrical stimulation circuitry directly on-chip, in turn allowing a high degree of flexibility in generating spatiotemporal patterns of stimulation owing to dense and flexible wiring, higher spatial resolution for stimulation owing to densely packed electrodes and room for on-chip circuitry to blank or suppress stimulation artifacts.

Electrical stimulation has been typically applied as a "trigger" for the so-called stimulus-triggered averaging (Cheney and Fetz 1985). By delivering electrical pulses through the microelectrode, action potentials (APs) can be triggered from nearby neurons, with an effective stimulation range depending on the neuron's distance from the stimulation site and the amplitude of the pulse. With HD-MEAs, stimulus-triggered averaging reveals the electrical activity footprint of a single neuron, that is, signals detected at the electrode sites corresponding to the EAPs from a single neuron, where negative spikes correspond to the AP initiated at the axonal initial segment and the positive spikes represent return current, including the propagation of APs in axons (Bakkum et al. 2013). The stimulation amplitude has to be sufficient to consistently evoke an AP with small temporal jitter (e.g., a jitter of 160 μs) (Bakkum et al. 2008). Figure 5a shows how small axonal signals, typically undetectable from noise, become observable by increasing the number of
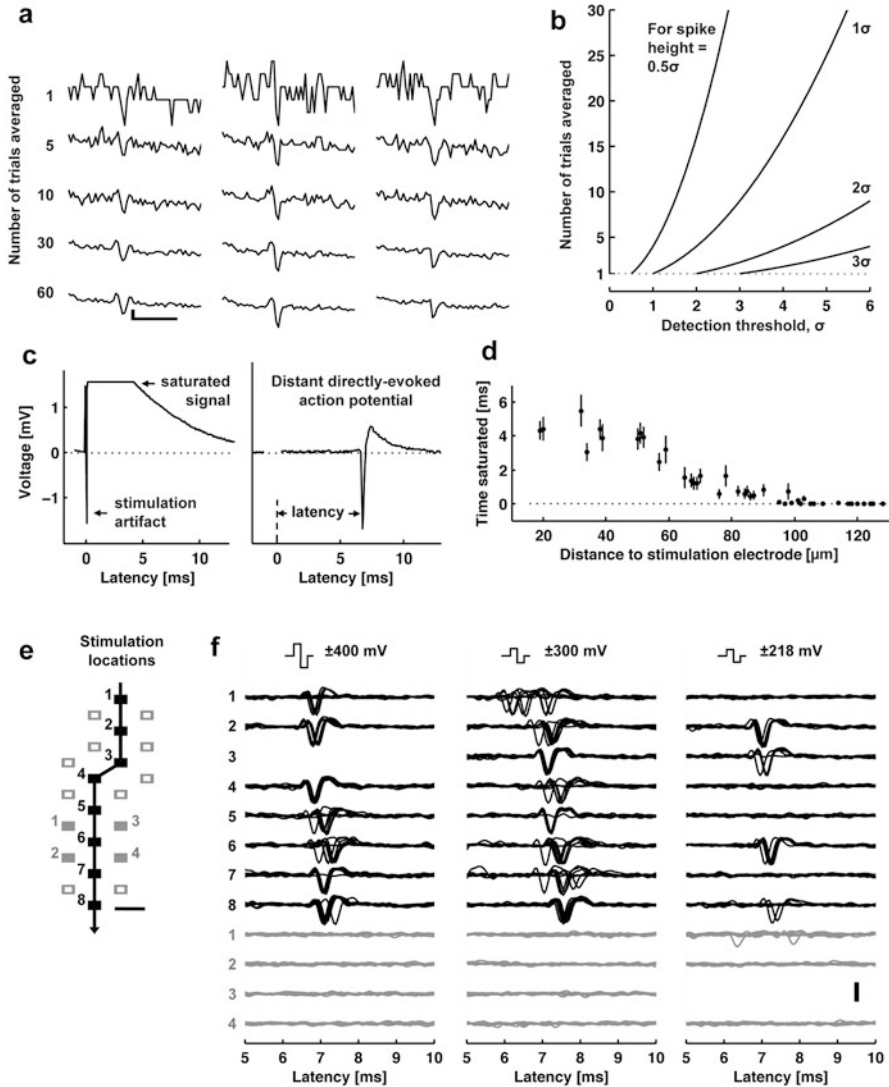
Fig. 5 Stimulation capability of HD-MEAs. (**a**, **b**) Stimulus-triggered averaging improves detection of axonal signals. (**a**) Evoked spikes detected at three chosen sites (columns) along the same axon. Each row shows individual traces obtained by increasing the number of averaged trials, from 1 to 60. Scale bars, 1 ms horizontal, 10 μV vertical. (**b**) The number of averaged trials necessary to detect a spike with a given height (0.5–3 times the standard deviation of the noise, σ) with respect to the detection threshold. (**c**, **d**) Electrical stimulation affects recorded signals of electrodes <100 μm away from the stimulation site. (**c**) Left: A raw trace recorded at an electrode neighboring a stimulation electrode (18 μm away) saturated for about 4 ms (flat line). Right: A raw trace recorded at an electrode located 1.46 mm away from a stimulation electrode did not saturate. (**d**) The duration of a saturated signal occurring after stimuli decreases with increasing distance from the stimulation electrode (mean ± s.e.m.; $N = 18$ stimulation electrodes from five HD-MEAs). Stimuli consisted of biphasic voltage pulses between 100 and 200 ms duration per

trials averaged. The number of trials that must be averaged depends on the spike amplitude as shown in Fig. 5b.

One issue of electrical stimulation is the occurrence of artifacts in the recording channels. Stimulation pulses are typically three to four orders of magnitude larger than the recorded EAPs; the recording channels can pick up the artifacts through the wiring in the circuitry or through the media to neighboring electrodes. If the artifact amplitude is large, the amplification circuits may saturate and this prevents recording neuronal activity until the offset settles back to normal. Figure 5c provides an example of signal saturation due to stimulation in a SM HD-MEA (Frey et al. 2010). A recording electrode near the stimulation electrode (18 μm away) saturated for around 5 ms; another electrode located far from the stimulation site (1.5 mm away) did not saturate. Figure 5d presents the relationship between the distance from stimulation to recording electrode and the duration of saturation for a 11,011-electrode MEA (Frey et al. 2010), without employing any artifact suppression measures. As long as the amplifiers do not fully saturate, artifacts can be suppressed via software by subtracting the estimated artifact (based on templates, filters or local curve fitting) from the data (Hashimoto et al. 2002; Wagenaar and Potter 2002). To also allow recording from electrodes on which saturation would occur, counter measures in hardware have to be employed. One solution is to use a "reset" switch that can bring back the saturated amplifier into normal operation quickly, by resetting the high-pass filter of the front-end amplifier (Frey et al. 2010; Heer et al. 2006).

Local delivery of stimulation pulses can be achieved by HD-MEAs. Figure 5e, f show stimuli activated neuronal responses with high spatiotemporal precision. In a study to track axonal APs (Bakkum et al. 2013; Radivojevic et al. 2016) several ten thousands of stimuli used for stimulus-triggered averaging did not damage the electrodes or the cells. Voltage-mode stimulation was used, although the stimulation hardware supported both current and voltage modes (Livi et al. 2010).

Combined recording and stimulation capabilities allow for performing closed-loop experiments, whereby recorded signals are programmed to control the application of electrical stimuli. In such experiments, spike detection is performed online, typically through a dedicated hardware, for example, a desktop with a real-time operating system or a field-programmable gate array (FPGA) (Hafizovic et al. 2007; Müller et al. 2013).
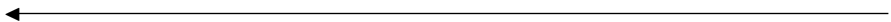
Fig. 5 (continued) phase and between ±400 and 800 mV amplitude. (**e**, **f**) Electrical stimulation can be delivered locally to axons and evoke action potentials. (**e**) Locations of stimulation electrodes that directly evoked (black boxes) or did not evoke (empty or filled gray boxes) APs detected at a soma located ∼890 μm away. The line arrow indicates the orthodromic propagation direction. Scale bar, 20 μm. (**f**) Voltage traces of somatic APs elicited by biphasic voltage stimuli. Traces in response to eight stimuli are overlaid for each of three stimulation magnitudes (indicated at the top), plotted for all effective (black) and four ineffective stimulation sites (gray at the bottom). Stimulation electrode locations are represented as numbered boxes in (**e**). Scale bar, 200 μV. All panels and description adapted with permission from Bakkum et al. (2013)

2.3   Performance of HD-MEAs

Here we discuss the main factors affecting the recording performance of MEAs: (a) neuron–electrode interface; (b) noise; (c) electrode size and density; and (d) recording hardware. Figure 6 illustrates the components of the MEA signal flow (Fejtl et al. 2006; Stett et al. 2003).
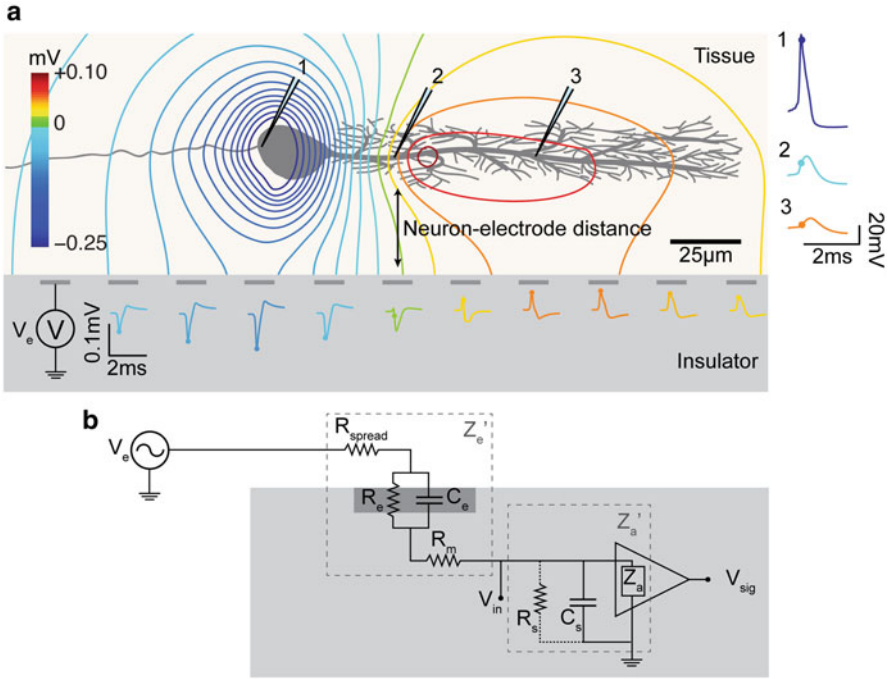
2.3.1   Effect of the Neuron–Electrode Interface

The early MEA neuron–electrode interface model assumed a tight seal between the neuron and the electrode (Weis and Fromherz 1997). However, extracellular microelectrodes can record EAPs and LFPs at a distance from active neurons, as observed in acute tissue and in vivo experiments. Likewise, for 2D neuronal networks grown on a MEA, EAPs can be detected from electrodes distant from the neuronal source. Thus, the neuron–electrode interface model can be separated into two parts (see Fig. 7): (1) the fluid side, which considers the effect of the volume conductor to the extracellular potential at the electrodes and (2) the metal side, which models the transformation of the extracellular potential through the electrode to the input of the front-end amplifier.

The distance and orientation of neurons with respect to measuring electrodes affect the amplitude and shape of the detected signals. The characteristics of the extracellular space, such as conductivity, anisotropy, and inhomogeneity, influence the spread of neuronal signals towards the electrodes. These effects can be estimated using the volume conductor theory illustrated in Fig. 7a. As a first order approximation, the MEA surface can be considered as an infinite insulating plane, while the tissue and/or fluid in the MEA dish can be assumed to be infinite, homogeneous, and isotropic. A neuron's membrane current can be decomposed into several point current sources. The method of images can then be applied to Coulomb's law to solve the potential V_e at any given electrode e in a volume conductor with conductivity σ (Ness et al. 2015; Obien et al. 2015):
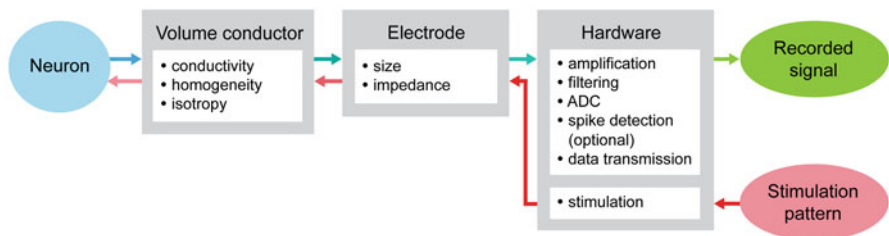
Fig. 6 MEA recording and stimulation system diagram. A neuron's signal, typically an action potential, is transduced through different components of the signal path into a digitally recorded trace. Similarly, a digital pattern generated from a computer or the MEA hardware applies current or voltage at the electrode during stimulation. Adapted with permission from Obien et al. (2015)

Fig. 7 MEA neuron–electrode interface divided into (**a**) fluid side and (**b**) metal side. (**a**) The potential at the electrode sites can be solved using the volume conductor theory. The MEA surface can be assumed as an insulator such that the method of images applies and can be used to solve the potential at any point on the MEA surface. The neuron–electrode distance and neuron orientation influences the signal amplitude and shape detected at the electrodes. High spatial resolution allows for recording EAPs at several locations of a single neuron, with large negative spikes at the perisomatic area and positive spikes at the dendritic area (i.e., return current). (**b**) The voltage measured at the electrode is transformed by the electrical parameters of the electrode–electrolyte interface, represented by Z_e' as the effective electrode impedance and Z_a' as the effective input impedance. This model is derived from Hierlemann et al. (2011), Nelson et al. (2008), and Robinson (1968). R_{spread}—spreading resistance; R_e and C_e—resistance and capacitance of the electric double layer at the electrode–electrolyte interface; R_m—resistance of the metallic part of the electrode; R_s and C_s—shunt resistance and capacitance. Adapted with permission from Obien et al. (2015)

$$V_e = \frac{1}{2\pi\sigma} \sum \frac{I_n}{r_n}.$$

I_n represents the nth point current source and r_n represents the distance between the point source and the recording electrode e, with $n = 1 \ldots N$, where N is the number of individual point sources. For electrodes larger than an ideal point electrode, V_e can be solved at multiple locations of the electrode's surface area and then averaged. This equation can be extended to include the anisotropy and inhomogeneity of brain

tissue, the saline layer above the tissue, and to use line sources instead of point sources to represent neuronal membrane currents (Ness et al. 2015).

2.3.2 Noise and SNR

One crucial aspect of the MEA signal flow is how noise is fed into the amplification chain and how it affects the signal-to-noise ratio (SNR) of the recorded data. SNR is the key specification for the amplifier design, regardless of the actual amplification (Jochum et al. 2009). There are several noise sources to consider in analyzing MEA recordings. It is important to consider where the noise, or interference, is injected in the signal chain, as the implications on SNR will differ.

Biological Noise A major source of noise comes from the electrical activity of other cells around the recording electrode (e.g., APs of distant cells) but also ionic activity (e.g., subthreshold events in neurites of nearby cells) and synaptic noise due to the stochastic nature of synaptic transmission. Several models of biological noise, or sometimes also called background noise, have been developed by simulating uncorrelated single-unit spiking activities or examining multicompartmental neuron models located at distances far enough away from the electrodes such that the spikes cannot be resolved (Camuñas-Mesa and Quiroga 2013; Eaton and Henriquez 2005; Jäckel et al. 2012; Lempka et al. 2011; Martinez et al. 2009). Although such models replicate the average biological noise in experiments, it is possible that the cell type, size, and morphology along with the firing rates and correlated activity can affect the shape of the background signal. For spike analysis, LFP is also considered biological noise and is filtered out.

Electrode–Electrolyte Interface Noise On top of biological noise, the liquid–metal interface also adds to noise. At low frequencies, such as below 10 Hz, processes at the electrode generate noise with a steep roll-off of *1/f* or even *1/f²* (Hassibi et al. 2004; Heer 2005). More relevant for electrophysiology are the frequencies above that, where thermal noise is the main contributor (Gesteland et al. 1959; Liu et al. 2007). The equivalent thermal noise can be calculated as follows:

$$v_n = \sqrt{4 \cdot k \cdot T \cdot \mathrm{Re}\left(Z_e'\right) \cdot \Delta f},$$

where k is the Boltzmann constant, T is the absolute temperature, $Re(Z_e')$ is the real part of the effective electrode impedance, and Δf is the noise bandwidth. Another source of noise is the 50–60 Hz hum from power lines. This noise is largely picked up between the microelectrode and the connection to the input of the preamplifier, due to its high impedance at that frequency. Hence, minimizing the distance between the electrode and the amplifier is a major design requirement for MEA circuits (Harrison 2008). Proper grounding and shielding of the MEA setup can minimize interference.

Device Noise The device or the system that amplifies and digitizes the signals further adds to noise. Usually, the front-end amplifier is the most important factor to consider. A general design objective for such amplifiers is to ensure that the signal acquisition system does not limit the system performance with regard to noise. As discussed above, this is a design trade-off in which also power and circuit area may play a role. For example, if the maximal allowed contribution to noise from the circuitry is set to 10%, the amplifier noise needs to be 45% or less as compared to the noise of the electrode. A commonly used figure of merit that captures the trade-off between noise and amplifiers' supply current is the noise efficiency factor (NEF) proposed in Steyaert and Sansen 1987. This figure has also been adapted to capture the different supply voltages used to allow for a better comparison with respect to power consumption, coining the term power efficiency factor PEF (Muller et al. 2012). For in vitro MEAs, area is also of critical importance, as it usually impacts electrode density and total channel count. The efficient use of the overall area is reflected in the ratio of the actual array area divided by the overall chip area (see Fig. 4). Quantization noise is another noise contributor of the hardware. It originates from the discretization error made at the ADC part of the MEA system. As an approximation for the quantization noise, typically a value of $\frac{1}{\sqrt{12}}$ times the magnitude of the least significant bit (LSB) is used. Typical ADCs used for MEA systems have a minimum of 8-bit resolution; systems that employ off-chip ADCs generally use 16-bit resolution. Finally, the transmission of data may also affect the quality of the recorded signal (e.g., if a lossy compression has to be used due to bandwidth constraints).

2.3.3 Effect of Electrode Size and Density

Sizes of published microelectrodes range from 5–50 μm in diameter (Kim et al. 2014) and even >50 μm. The most evident contribution of electrode size to SNR is the electrode impedance $Z_e{}'$, which in turn determines electrode noise. Large electrodes (>50 μm) have a positive effect on the SNR due to low impedance. Moreover, large electrodes have a higher possibility of getting physically near the neurons and of picking up higher amplitude spikes (Camuñas-Mesa and Quiroga 2013); for example, studies by Andersen et al. (2010), Moxon (1999), Paik et al. (2003), and Ward et al. (2009) claim that larger recording electrodes can record from more neurons simultaneously. However, the detected amplitude of a large EAP signal from a neuron is reduced as it is averaged out by nearby smaller amplitude signals, thus resulting in a lower SNR. Sorting all the signals detected by a single large electrode to their respective individual sources can also be daunting when many neurons are nearby.

For recording EAPs, especially for dissociated cell culture experiments, the use of small electrodes (<15 μm diameter) minimizes averaging. Small electrodes are inferior against large electrodes in terms of impedance, but this can be improved by surface modification. For example, the influence of electrode size (<10 μm
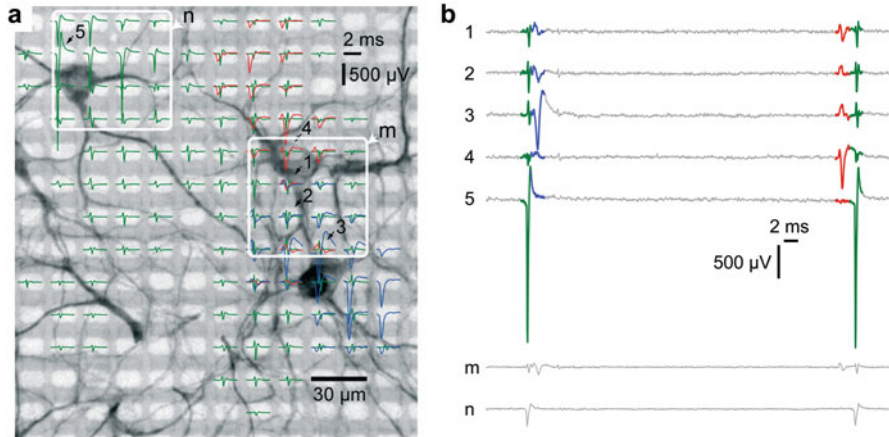
Fig. 8 Comparison of the recording capability of small electrodes at high-density and large electrodes. (**a**) The EAPs of three identified neurons (green, red, and blue) detected from each electrode site (light gray rectangles) are superimposed to a fluorescence image (MAP 2 staining) of a cell culture on a HD-MEA. Each spike represents the spike-triggered average over 50 trials. Spikes with amplitude below 50 μV are not shown. White squares represent the location of hypothetical large electrodes (60 × 60 μm) used for comparison of signals. (**b**) Raw traces from small electrodes (1–5) and large electrodes (m, n) indicated in (**a**). Signals for the large electrodes (m, n) are estimated by averaging the traces of the small electrodes within the area covered by the white squares. Estimated signals from (m, n) show reduced amplitudes due to the averaging effect only. The impedance effect due to electrode size differences may be neglected due to high input impedance at the first-end amplifier of the HD-MEA, and is thus not considered. Modified with permission from Müller et al. (2015)

diameter) on recorded signal amplitude significantly decreases by depositing Pt-black on platinum microelectrodes (Viswam et al. 2014). HD-MEAs have small electrodes to allow the integration of a large number of sensors in an array. The dense grid of electrodes in HD-MEAs, shown in Fig. 8, increases the possibility of having an electrode "at the right spot" while also allowing a single neuron to be recorded from multiple electrodes. Also, the effective input capacitance can be significantly smaller in HD-MEAs as compared to passive devices, due to a small C_s, which in turn allows for a smaller C_e (see Fig. 7b and the next subsection for more information). As a result, small electrodes are much more preferable in this situation, with only electrode noise being the limiting factor.

For LFP recording, Nelson and Pouget (Nelson and Pouget 2010) discussed that the electrode impedance and recording site geometry are not crucial. This is because LFPs only vary in a spatial scale much larger than the size of electrodes used for extracellular recordings, for example, by a few hundred micrometers (Katzner et al. 2009) or even by 1 mm (Destexhe et al. 1999). In addition, LFPs are of lower temporal frequency, making electrode noise a more important factor as in that range, it is dominated by $1/f^2$ noise, which makes larger electrodes more favorable.

Novel 3D microstructure and nanostructure electrodes aim to detect subthreshold neuronal signals (e.g., synaptic potentials, membrane oscillations) and membrane potentials (Spira and Hai 2013). These subthreshold signals cannot be detected by MEAs; these signals are conventionally measured using patch clamp. The 3D electrodes seek to achieve either a tight seal with the neuronal membrane or to temporarily puncture into the membrane and access the intracellular space of a neuron. With advancements in fabrication techniques, large-scale integration of 3D microelctrodes and nanoelectrodes is feasible on HD-MEAs (Dipalo et al. 2018).

It is therefore important to choose optimal electrode sizes depending on the targeted application. In addition, a high density of electrodes will inherently limit the electrode size.

2.3.4 Effect of the Recording Hardware

HD-MEA circuitry includes amplifiers, filters, and some sort of data transmitter of either the amplified analog signals or, more typically, of the already digitized data. The front-end amplifier has a major effect in the performance of the HD-MEA. It needs high input impedance to ensure signal quality.

A neuronal signal is transduced by an electrode into a current, and this process depends on the parameters of the effective electrode impedance Z_e' and effective input impedance Z_a'. We discuss this using the equivalent circuit of the electrode–electrolyte interface shown in Fig. 7b. Noise (e.g., thermal noise and power line hum) can be injected into the recorded signal at the liquid–metal interface. Z_e' is the total impedance due to R_{spread}, R_e, C_e, and R_m. R_{spread} represents the effect of the electrode geometry and liquid conductivity. R_e and C_e are the resistance and capacitance of the electrode double layer formed at the electrode–electrolyte interface. R_m is the resistance of the metallic part of the electrode. Connected in series to Z_e' is Z_a', which is mostly influenced by the input impedance of the front-end amplifier Z_a and the shunt capacitance C_s. C_s includes the capacitances from connectors and wires from the liquid to the amplifier. The shunt resistance R_s is usually negligible. All these represent the metal side of the neuron–electrode interface. For more details on the circuit model, see Hierlemann et al. (2011), Nelson et al. (2008), and Robinson (1968).

Front-end amplifiers are designed to have large Z_a' in order to preserve signal quality. The ratio between Z_e' and Z_a' shows how to derive the voltage at the input of the amplifier as (Nelson et al. 2008):

$$V_{\text{in}}(\omega) = \frac{V_e(\omega)}{1 + \left(Z_e'(\omega)/Z_a'(\omega)\right)},$$

where $V_e(\omega)$ is the total extracellular potential at the electrode, $V_{\text{in}}(\omega)$ is the voltage at the input of the front-end amplifier. V_{in} will be smaller than V_e, that is, the signal will be attenuated if Z_a' is not substantially larger than Z_e'.

In addition to the effect of the input impedance, the circuitry near the cells must be low powered in order to prevent heating that could damage the cells. Appropriate settings for gain and dynamic range of the readout depend on the preparation (e.g., maximum amplitudes of a few hundred microvolts in acute slice preparations and up to 10 mV in cardiomyocyte experiments). The recording bandwidth needs to be flexible to cover both LFP and EAP frequency ranges, depending on the experiment, in order to avoid filtering out signals of interest.
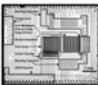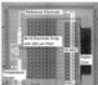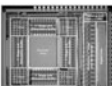
Many of the circuit requirements can be traded against each other; for example, one can easily lower the noise by increasing the area or power consumption. The key challenge therefore is to set the target specifications for the given application accurately and optimize the systems for it, without overdesigning specific requirements.

3 Applications of HD-MEAs

In this section, we discuss specific neuroscience studies from selected experiments. Measurements done using passive MEAs can also be done using CMOS-based HD-MEAs. However, the high spatiotemporal resolution of HD-MEAs leads to novel types of data that were not possible to collect using conventional MEA devices.

In recent years, CMOS-based MEAs have been increasingly used for neuroscience and biomedical research. Figure 9 lists the currently available CMOS-based in vitro MEAs, their key specifications, and some experimental preparations for which they have been applied so far. The two most prominent preparations investigated using these devices are dissociated cell cultures from snails (Eversmann et al. 2003), rats (Bakkum et al. 2013; Gandolfo et al. 2010; Hafizovic et al. 2007; Heer et al. 2007; Lambacher et al. 2010; Lewandowska et al. 2015, 2016; Müller et al. 2015) and chicken (Hafizovic et al. 2007) and acute retina from mice (Fiscella et al. 2012, 2015; Franke et al. 2016; Maccione et al. 2014; Menzler and Zeck 2011; Yonehara et al. 2016), rats (Eickenscheidt et al. 2012; Lloyd et al. 2014; Stutzki et al. 2014), rabbits (Ballini et al. 2014; Fiscella et al. 2014; Zeck et al. 2011), hamsters (Jones et al. 2015), guinea pigs (Bertotti et al. 2014; Velychko et al. 2014), and humans (Reinhard et al. 2014). Additionally, data from acute slices of cerebellum (Frey et al. 2009a; Obien et al. 2014), cortex (Ferrea et al. 2012; Medrihan et al. 2014), and olfactory bulb (Johnson et al. 2013a) have been presented. Cultured cardiomyocytes were also studied (DeBusschere and Kovacs 2001; Heer et al. 2004; Huys et al. 2012; Imfeld et al. 2008; Sanchez-Bustamante et al. 2008), and first results from mice organotypic hippocampal slices were presented (Gong et al. 2016). This section reviews recent neuroscience applications of HD-MEAs.

Ref	Micrograph	Key Specs	Published Recordings	Published Stimulation
APS (Eversmann et al., 2003) Other versions: (Eversmann et al., 2011)		• Technology: 0.5μm • Chip area: 35mm^2 • Array area: 1.0mm^2 (2.9%) • Rec. sites: 16384 (OSFET) • Stim. sites: 0 • Channels: 16384 • Trans. density: 16384mm^{-2} • Power: 656mW	• Acute (Rr, Mr, Lr): (Menzler and Zeck, 2011; Stutzki et al., 2014; Zeck et al., 2011) • Cultures (S, Rc): (Eversmann et al., 2003; Lambacher et al., 2010)	• Acute (Lr): (Eickenscheidt et al., 2012)
APS (Heer et al., 2006) Other versions: (Heer et al., 2004)		• Technology: 0.6μm • Chip area: 42mm^2 • Array area: 8.0mm^2 (19%) • Rec. sites: 128 (Pt) • Stim. sites: 128 (Pt) • Channels: 128 • Trans. density: 16mm^{-2} • Power: 120mW	• Cultures (Cch, Rc): (Hafizovic et al., 2007; Heer et al., 2007, 2004)	• Cultures (Rc): (Hafizovic et al., 2007)
APS (Imfeld et al., 2008) Other versions: (Berdondini et al., 2005;		• Technology: 0.35μm • Chip area: 29mm^2 • Array area: 7.2mm^2 (25%) • Rec. sites: 4096 • Stim. sites: 16 (newer versions) • Channels: 4096 • Trans. density: 567mm^{-2} • Power: 132mW	• Acute (Mcr): (Ferrea et al., 2012; Maccione et al., 2014; Medrihan et al., 2014) • Cultures (Rch): (Gandolfo et al., 2010; Imfeld et al., 2008)	• Cultures (Rc): (Maccione et al., 2013)
SM (Frey et al., 2009)		• Technology: 0.6μm • Chip area: 46mm^2 • Array area: 3.5mm^2 (7.6%) • Rec. sites: 11011 (Pt) • Stim. sites: 11011 (Pt) • Channels: 126 • Trans. density: 3150mm^{-2} • Power: 135mW	• Acute (Rpr, Lr, Hr, Mpr): (Frey et al., 2009; Fiscella et al., 2012, 2014, 2015; Jones et al., 2014, 2015; Obien et al., 2014; Reinhard et al., 2014; Franke et al., 2016) • Cultures (Rh, Rc): (Sanchez-Bustamante et al., 2008; Bakkum et al., 2013; Lewandowska et al., 2015, 2016) • Organotypic (Mc): (Gong et al., 2014)	• Acute (Rr): (Lloyd et al., 2014) • Cultures (Rc): (Bakkum et al., 2013)
SM (Huys et al., 2012)		• Technology: 0.18μm • Chip area: 64mm^2 • Array area: 14.7mm^2 (23%) • Rec. sites: 16384 (W) • Stim. sites: 16384 (W) • Channels: 1 • Trans. density: 1111mm^{-2} • Power: 35mW	• Cultures (Rh): (Huys et al., 2012)	• Cultures (Rh): (Huys et al., 2012)
APS (Johnson et al., 2013a) Other versions: (Johnson et al., 2013b)		• Technology: 0.18μm • Chip area: 4mm^2 • Array area: 2.8mm^2 (70%) • Rec. sites: 1120 (Al/Pt) • Stim. sites: 0 • Channels: 1120 • Trans. density: 400mm^{-2} • Power: 14.1mW	• Acute (Mo): (Johnson et al., 2013a)	
SM (Ballini et al., 2013)		• Technology: 0.35μm • Chip area: 77mm^2 • Array area: 8.1mm^2 (11%) • Rec. sites: 26400 (Pt) • Stim. sites: 26400 (Pt) • Channels: 1024 • Trans. density: 3265mm^{-2} • Power: 75mW	• Cultures (Rc): (Ballini et al., 2014; Müller et al., 2015) • Acute (Mr): (Yonehara et al., 2016)	• Cultures (Rc): (Ballini et al., 2014; Müller et al., 2015)
APS (Bertotti et al., 2014)	Not available	• Technology: 0.18μm • Array area: 4.3; 1.1mm^2 • Rec. sites: 4225 (OSFET) • Stim. sites: 1024 (CAP) • Channels: 4225 • Trans. density: 977; 3906mm^{-2}	• Acute (Gr): (Bertotti et al., 2014)	• Acute (Gr): (Bertotti et al., 2014)
SM (Viswam et al., 2016)		• Technology: 0.18μm • Chip area: 106.8mm^2 • Array area: 10.9mm^2 • Rec. sites: 59760 (Pt) • Stim. sites: 59760 (Pt) • Channels: 2048 (AP)+32(LFP) • Trans. density: 5487mm^{-2}	• Cultures (Rc): (Viswam et al., 2016)	• Cultures (Rc): (Viswam et al., 2016)

M: Mouse, R: Rat, H: Human, L: Rabbit, C: Chicken, G: Guinea pig, S: Snail
r: Retina, p: Cerebellum, o: Olfactory bulb, c: Cerebral cortex/hippocampus, h: Cardiomyocytes

Fig. 9 CMOS-based in vitro MEAs, their key specifications and references to biological applications for recording and stimulation. The specifications may differ for other device versions. Modified with permission from (Obien et al. 2015)

3.1 Electrical Imaging

HD-MEAs can be used to monitor the electrical activity of neurons in a cell culture or tissue preparation at high-resolution, thus termed here as *electrical imaging*. Examples of electrical imaging of a cell culture are shown in Fig. 2. The whole sample can be electrically imaged to create activity or amplitude maps of active neurons. Moreover, HD-MEAs with low noise can reveal subcellular resolution maps of single neurons.

Similarly, electrical imaging can be performed for 3D samples, such as acute brain slices. Two types of electrical images can be obtained: (a) based on EAPs shown in Fig. 10 and (b) based on LFPs presented in Fig. 11. The neurons and network structure in slices are physiologically and biochemically similar to the in vivo situation.

Depth recording of EAPs from neurons up to 100 μm distance from the MEA surface has been shown (Egert et al. 2002; Frey et al. 2009b). In Fig. 10 we show a demonstration of subcellular resolution electrical imaging of single Purkinje cells (PCs) in acute cerebellar slices (Frey et al. 2009a). To ensure the quality of recorded signals, proper tissue adhesion on the MEA surface has to be maintained throughout the experiment (Egert et al. 2002). EAPs were observed along the PC layer, and, after spike sorting, the EAP footprint of a single PC was analyzed. The negative spikes were recorded around the perisomatic area of the neuron, while positive spikes were obtained along the molecular layer corresponding to the dendrites of the PC.

Large LFPs and oscillations inherent in different states of the brain can also be imaged at longer time scales. Such recordings have been done for different brain areas (e.g., hippocampus and suprachiasmatic nucleus). HD-MEAs can easily capture electrical images of neuronal network activity in slices. For instance, functional imaging of the dentate gyrus has been demonstrated using HD-MEAs (Ferrea et al. 2012). Field excitatory postsynaptic potentials (fEPSPs) evoked by electrical stimulation were detected across different layers of the acute slice, as shown in Fig. 11.

3.2 Axonal Studies

HD-MEAs with high SNR, such as SM HD-MEAs (Frey et al. 2010; Müller et al. 2015), allowed for detection and tracking of APs propagating along a neuron's axon for the first time (Bakkum et al. 2013), and more recent studies continue to be performed (Radivojevic et al. 2016, 2017). Axonal signals are difficult to measure using conventional methods—thin axons are challenging to patch, and extracellular signal amplitudes are low compared to those from the soma and axon initial segment. In this work, the propagation of APs along the full arbor of a neuron has been electrically imaged, shown in Fig. 12a–c. Subsequently, axonal AP velocity
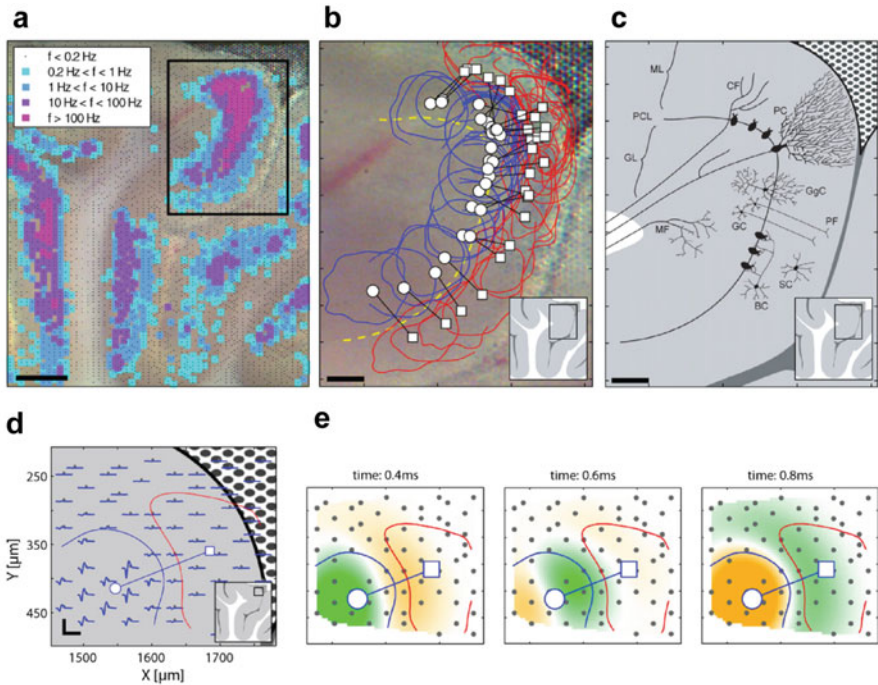
Fig. 10 High-resolution electrical imaging of spontaneous cerebellar Purkinje cell activity using HD-MEAs. (**a**) Activity map of the detectable spike activity in the recording area. Small dots correspond to the electrodes used for recording (∼30% of the available electrodes). Events exceeding a threshold of ±36 μV were used to calculate the color-coded event rate. Scale bar: 0.3 mm. (**b**) Close-up of a region with high activity delimited in (**a**). All units identified by spike sorting are marked, that is, the somatic region is blue and the dendritic region is red. Scale bar: 0.1 mm. (**c**) Schematic of the basic cellular structures in the cerebellar slice (Gray et al. 1918). Scale bar: 0.1 mm. *ML* molecular layer, *PCL* Purkinje cell layer, *GL* granular layer, *CF* climbing fiber, *MF* mossy fiber, *PF* parallel fiber, *PC* Purkinje cell, *GgC* Golgi cell, *SC* stellate cell, *BC* basket cell. (**d**) Footprint of a PC selected from the region shown in (**b**). Scale bar: vertical is 200 μV, horizontal is 1.9 ms. (**e**) Current source density (CSD) analysis for the cell shown in (**d**) at several points in time (green: sink; yellow: source). The sink moves from the soma at 0.4 ms to the proximal dendrites at 0.6 ms and covers the dendritic area, while the soma repolarizes. Frequency band: 180–3.5 kHz. (**f–h**) Matching simulated and measured EAP footprints. All panels and descriptions adapted with permission from Frey et al. (2009a)

was found to vary within single axons, hinting that axon velocity might contribute to temporal coding schemes of neuronal information. This capability can help expand new fields of research, such as axonal information processing and neuronal computation. Tracking the velocity of axonal signals also provides a new and promising parameter that can be used for analyzing the effect of different therapies (e.g., drugs and prolonged electrical stimulation) on the information transfer and signaling between neurons.
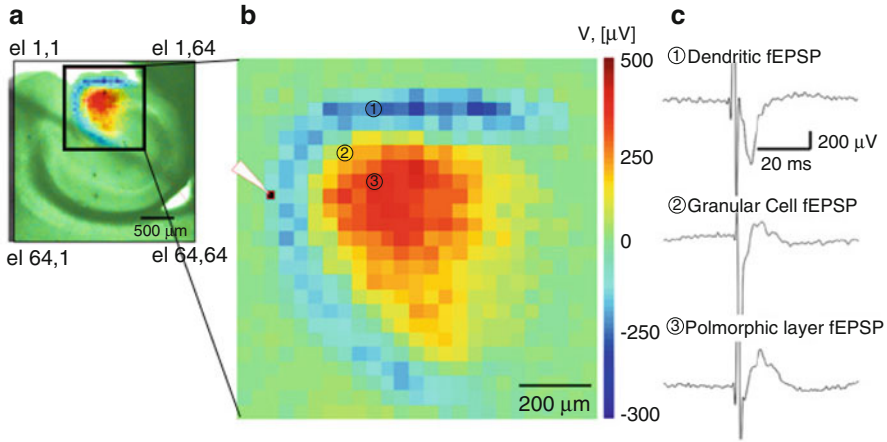
Fig. 11 Imaging network waves in acute hippocampal slices. (**a–c**) Functional imaging of the dentate gyrus, adapted with permission from Ferrea et al. (2012). (**a**) A corticohippocampal slice placed atop an APS HD-MEA, with superimposed color-coded fEPSP activity. (**b**) Close-up on the activated area in (**a**). The white tip indicates the site of stimulation using a patch pipette. (**d**) Recorded traces of fEPSPs from three chosen electrodes indicated in (**b**). Electrode 1 is located in the dendritic layer of the dentate gyrus, electrode 2 in the granular cell layer, and electrode 3 in the polymorphic layer

HD-MEAs have also been used for precise microstimulation. By taking advantage of the high electrode density, the responses of neurons to different stimulation patterns and intensity can be investigated, including how best to selectively stimulate single neurons (Radivojevic et al. 2016), as shown in Fig. 12d–f. Characterization of how stimulation affects neurons can benefit the design of stimulation therapies for clinical use.

Other studies amplify the axonal signals by growing the axons through polydimethylsiloxane (PDMS) microtunnels (Habibey et al. 2017; Lewandowska et al. 2015, 2016). PDMS tunnels were attached on top of an HD-MEA and cultured cortical neurons on each side of the tunnels. In time, many axons naturally enter and grow through the tunnels. While axonal signals outside of tunnels were also detectable, tunnels amplify the signals enough to avoid the need to average across trials and single axonal APs can be observed. By recording the spontaneous activities of the neurons, axonal signals were significantly amplified by a factor of 20–150.

3.3 Characterization of Novel Cell Types

Emerging breakthroughs in cell biology aim to provide in vitro platforms for preclinical drug screening and therapy diagnostics. In particular, human induced
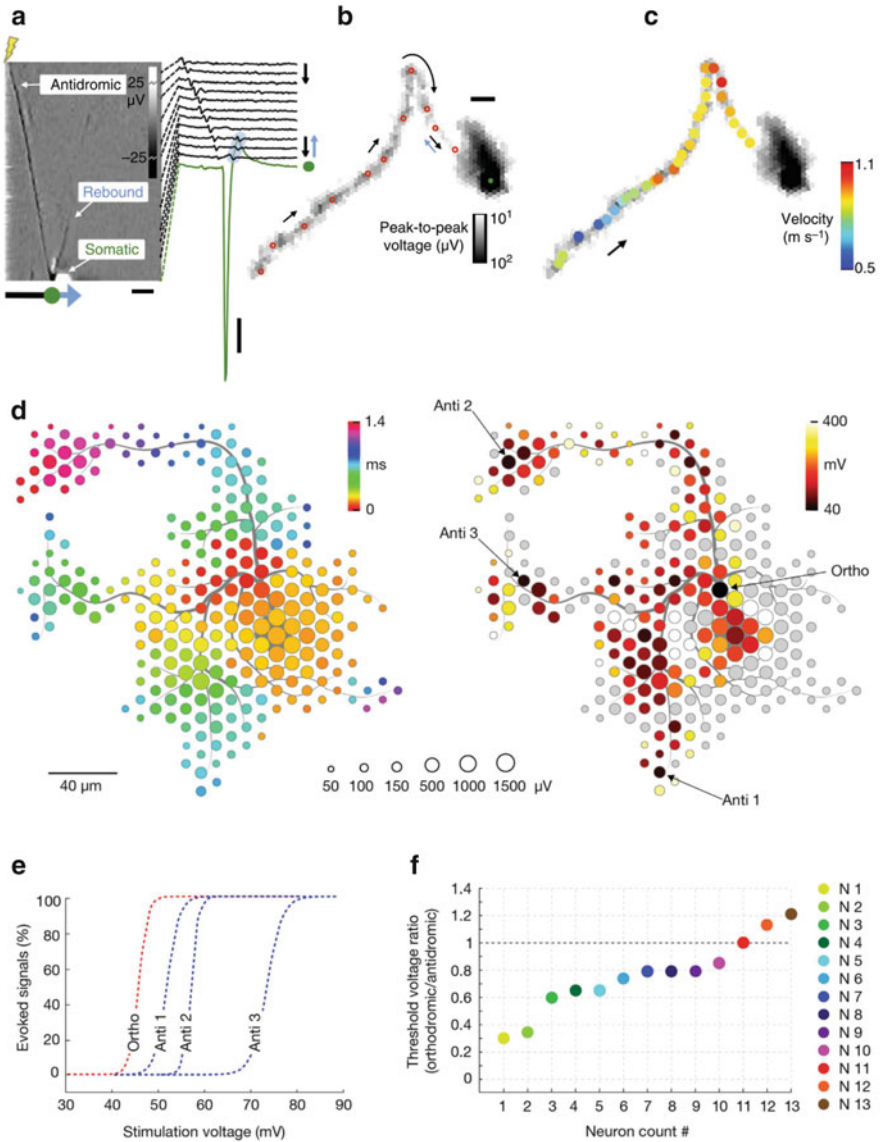
Fig. 12 Triggering and tracking axonal signals with HD-MEAs. (**a–c**) Adapted with permission from Bakkum et al. (2013). (**a**) Antidromic action potential triggered by electrical stimulation at the axon. Left: Heat map shows stimulation-triggered averages of 60 traces from 95 electrodes. Dark colored line from top to bottom indicates the antidromic propagation of an AP from the stimulation site. A subsequent rebound from the soma is also visible. Right: A subset of averaged raw traces. Scale bars, 1 ms horizontal; 100 μV vertical (**b**) The electrical footprint of the stimulated neuron recorded in (**a**). The gray scale pixels indicate the maximum peak-to-peak amplitude of the APs detected at each electrode. The red circles denote the locations of the subset of traces in A. The black arrows show the direction of the AP propagation along the axon, while the blue arrow indicates the subsequent rebound. The green dot is the location where the green trace in (**a**) was

pluripotent stem cell or hiPSC technology enabled to access human cells for in vitro investigation and to model diseases. HD-MEAs allow for efficient readout of hiPSC-derived neurons and cardiomyocytes for functional analysis. Culturing hiPSC derived neurons on HD-MEAs has been proven feasible and the cells remained viable up to 3 months (Amin et al. 2016). Spontaneous activity and responses to electrical stimulation were characterized. The authors found that spontaneous spiking activity of hiPSC derived neurons peaked around 81 DIV and that hiPSC derived neurons responded to electrical stimulation only at 90 DIV. Low-frequency electrical stimulations (0.2 Hz, biphasic current with peak-to-peak amplitude of 300 μA) led to an increase in the number of active electrodes (i.e., from 564 ± 28 to 688 ± 21) but decreased the mean firing rate (i.e., 0.66 ± 0.03 to 0.58 ± 0.03 spikes/s). Figure 13 summarizes these results.

The recent advent of CRISPR/Cas9-mediated genome editing has paved the way for fast development of disease models (Doudna and Charpentier 2014). Mice models of human diseases can be used to characterize the functional differences of cells from different parts of the body compared to their healthy counterparts. HD-MEAs can provide high-throughput and high-quality characterization of cells in culture and in acute preparations. One application of such characterization is biomarker identification, which has been done for a human retina disease called congenital nystagmus caused by FRMD7 gene mutation (Yonehara et al. 2016). A mouse model of such disease was developed, and light stimulation-evoked responses of RGCs in the retina were recorded and analyzed in a high-throughput manner. Using HD-MEAs, it was found that FRMD7 mutation leads to selective loss of horizontal selection selectivity of RGCs, as illustrated in Fig. 14.

3.4   Closed-Loop Studies

SM HD-MEAs enable simultaneous stimulation and recording of arbitrarily selected neurons in a network. By changing spike timing between sets of neurons via electrical simulations, the functional network connectivity was also changed (Müller et al. 2013). In this study, a reprogrammable event engine unit was programmed into

---

Fig. 12 (continued) recorded from. Scale bar, 100 μm. (**c**) AP propagation velocity changes, as shown by the colored dots along the electrical image of the axon. (D-F) Adapted with permission from Radivojevic et al. (2016). (**d**) Left: A single neuron's spike-triggered average footprint. Circle sizes correspond to logarithmically scaled amplitudes of APs and colors indicate spike time delay (negative peak) with respect to the spike initiation time of the respective neuron. Right: Stimulation map over the neuron's spike-triggered average footprint. Site-specific stimulation thresholds are color-coded; sites that were stimulated but did not evoke an action potential are colored in gray. Four sites are labeled "Anti 1–3" and "Ortho," indicating antidromic and orthodromic stimulation sites, respectively. (**e**) Excitability profiles of Anti 1–3 and Ortho sites. (**f**) Stimulation thresholds for the most sensitive orthodromic and antidromic sites determined for 13 neurons

Fig. 13 Spontaneous activity of hiPSCs. Recorded extracellular signal traces show changes in firing rates during development. The activity develops from single spikes (8 DIV), tonic firing (28 DIV) to bursting, and synchronized spikes (81, and 90 DIV). Red arrows denote the start of propagating burst. Adapted with permission from Amin et al. (2016)
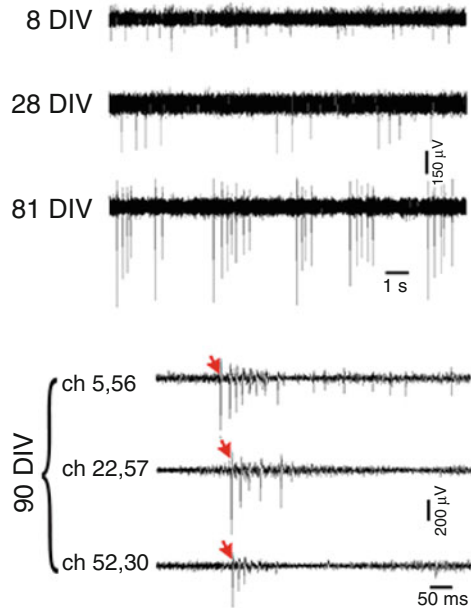
a field-programmable gate array. The system can detect arbitrary action potential patterns and use these to trigger electrical stimulations to arbitrary neurons, providing flexible and submillisecond latency closed-loop feedback. Cross-correlation analysis of spike trains showed the spike timing of the selectively stimulated neurons changed, which indicated that plasticity was induced in the network (Fig. 15).

3.5 Combination with Patch Clamp

The combination of HD-MEA and patch-clamp techniques provides a powerful approach to map monosynaptic connectivity of neurons in vitro. In such a combination, a single neuron or multiple neurons can be patched to detect subthreshold signals, such as postsynaptic potentials (PSPs), while the HD-MEA can be utilized to activate individual neurons by electrical stimulation. This method can be effectively applied to investigate local network mechanisms. First results have been obtained by Jäckel et al., showing contributions of presynaptic neurons, both excitatory and inhibitory, to PSPs (Jäckel et al. 2017), see Fig. 16. This combination technique can also be applied to brain slices; however, as cells are not directly attached on electrodes, higher stimulation amplitudes may be needed to evoke action potentials, which may activate multiple neurons at once. Additionally, the combined methods can enable imaging of a neuron's extracellular potential signature at subcellular resolution while controlling the cell's membrane potential.
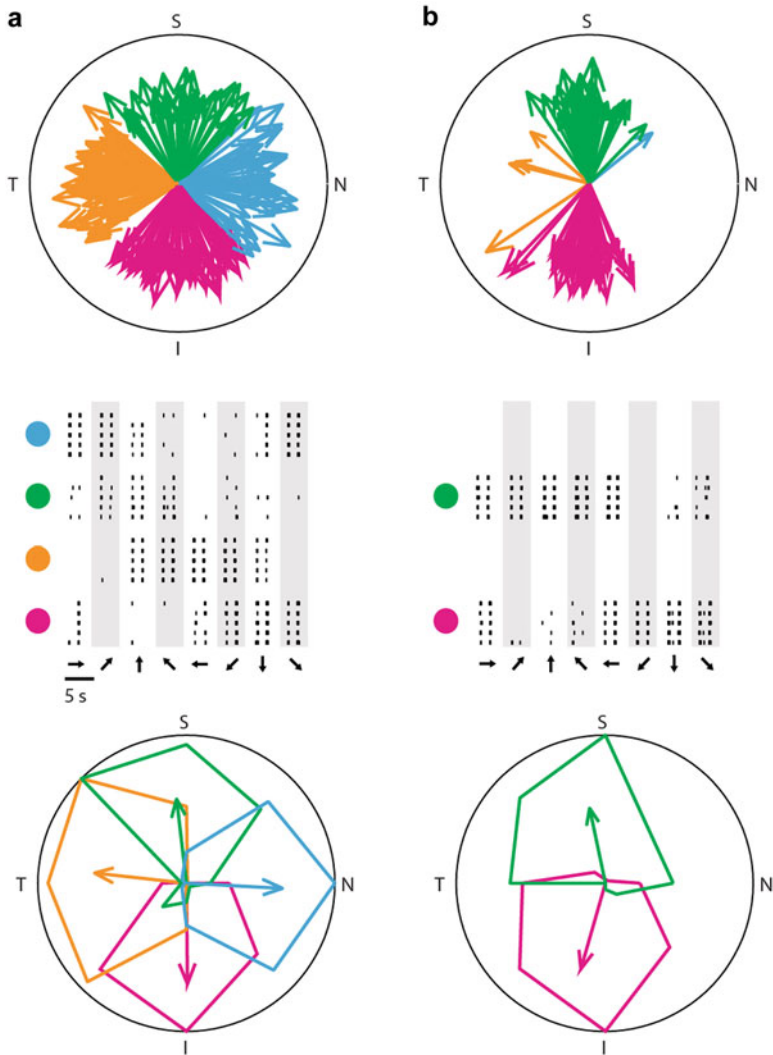
Fig. 14 Screening transgenic mouse models of human eye diseases with HD-MEAs. Top: Polar plots showing the preferred directions (directions of arrows) and direction selectivity index (length of an arrow) of individual direction-selective retinal ganglion cells in (**a**) WT and (**b**) FRMD7[tm] retinas. The color code shows the different preferred directions (green = superior, blue = nasal, purple = inferior, and orange = temporal). (Middle: Raster plots showing the spike responses (each black line is a spike) of example DS cells in WT and FRMD7[tm] retinas in response to motion in eight different directions, indicated by the arrows at the bottom of the plot. Bottom: polar plots of the normalized mean spike numbers of cells shown in middle panes. The preferred direction and DSI of each cell are represented by the direction and length of the corresponding (color-coded) arrow. Adapted with permission from Yonehara et al. (2016)
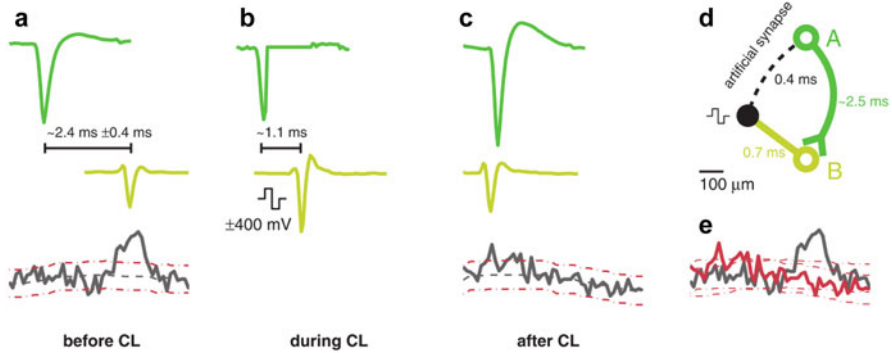
Fig. 15 Effect of closed-loop stimulation. (**a**) Spontaneous activity of two neurons before the application of the closed-loop stimulation. Spike traces are median waveforms of several spikes aligned at the negative peak. Top: In green, spike trace from neuron A, the trigger neuron. Middle: In yellow, spike trance of neuron B, a neuron with correlated spiking activity. Bottom: Cross-correlation curve of spike times of neuron B with respect to neuron A. Red dotted lines denote the 95% confidence intervals. Around 2000–3000 spikes were used to compute the cross-correlation. Elevated correlated activity of neuron B was observed around 2.4 ± 0.4 ms after neuron A fired an AP. (**b**) Same as (**a**), but with closed-loop feedback stimulation applied. The time delay of the spikes between neurons A and B was reduced to around 1.1 ms. Stimulation is applied upon detection of a spike from neuron A. During stimulation, the trace of neuron A was zeroed out. (**c**) Same as (**a**), but after application of the closed-loop stimulation. The cross-correlation plot changed after closed-loop stimulation. (**d**) Schematic of the synaptic connectivity between neurons A and B and the artificial synapse caused by closed-loop stimulation. (**e**) Comparison between the cross-correlation curves before (black) and after (red) the closed-loop stimulation. Adapted with permission from Müller et al. (2013)

Future developments of the technology may lead to electrically guided automated intracellular recordings (Annecchino et al. 2017; Kodandaramaiah et al. 2012, 2014; Suk et al. 2017).

Besides patch clamp, combining HD-MEA recordings with single-cell-targeted methods via a movable micropipette allows for advanced electrophysiology experiments (e.g., local puffing of compounds (Engle et al. 2012; Sasaki 2013; Sasaki et al. 2011), virus-stamping (Schubert et al. 2018), and single-cell electroporation (Boudes et al. 2008; Nevian and Helmchen 2007; Tanaka et al. 2009)). Such combination techniques will enable a detailed analysis of single cells in functional neuronal networks. Moreover, pipette-based dye-loading (Eilers and Konnerth 2009) can be used to obtain morphologies of recorded cells on the HD-MEAs. This enables acquisition of comprehensive information from defined cells towards developing precise and realistic multicompartment models.
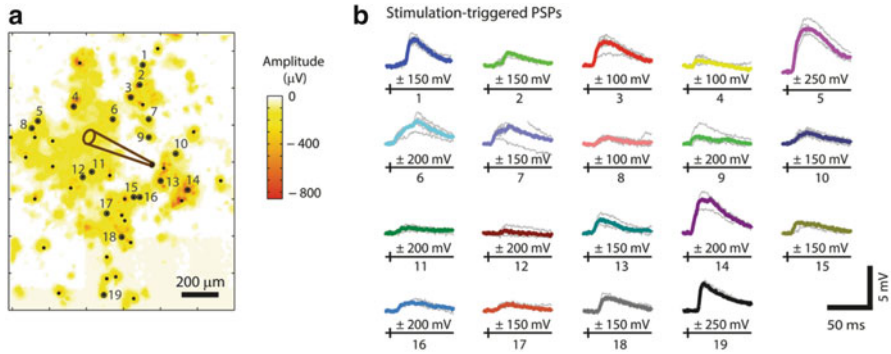
Fig. 16 Mapping synaptic connectivity through a combination of patch clamp and HD-MEA. (**a**) Amplitude map of the spontaneous activity of neurons with selected neurons marked with dots and numbered. The unselected neurons (unnumbered dots) did not evoke any postsynaptic potential (PSP) response. Each selected neuron was stimulated with bipolar voltage pulses ranging from 100 to 250 mV amplitude. The location of a single patched neuron is also shown. (**b**) PSP responses of the patched neuron (gray: individual traces; colored: median traces) to stimulation of individual presynaptic neurons. The minimum voltage values needed to evoke PSPs per presynaptic neuron are shown below the traces. The stimulus timing is also shown below the traces. Adapted with permission from (Jäckel et al. 2017)

4 Outlook

This chapter shows the current state of CMOS-based HD-MEA research in terms of technology and applications. Novel types of data can be obtained, which opens up new waves of possibilities for neuroscience discoveries and medical advancements. Potential future developments include device hardware improvements, advanced experimental methods, and new data analysis techniques.

Next generation HD-MEAs may target increased array area, electrode density, and number of parallel recording/stimulation channels. A larger array area will extend the observable region of a sample, allowing for simultaneous access to more neurons in cell cultures and to more distal brain areas in slices. This also enables opportunities for coculturing different tissues or brain regions. Higher spatial resolution and more recording channels will assist spike-sorting accuracy and will potentially increase the number of detectable neurons per square millimeter. Multiple HD-MEAs can also be combined in a multiwell-plate format, making HD-MEAs compatible to applications in drug discovery and development.

Aside from improving the devices through resolution and scalability, adding new functionalities may also be done. Other readout circuitry may also be integrated in HD-MEA devices (e.g., neurotransmitter and impedance measurement units) (Dragas et al. 2017). Multimodal measurement of neuronal activity will be helpful to understand the overall neuronal network function and the interplay between electrical activity and biochemical release.

Another promising route is the combination of HD-MEA with different tools separate from the device, such as optical methods. Fluorescent calcium and voltage indicators, generic markers, and optogenetics have been used to map and manipulate brain activity. Similar to extracellular recordings, the presence of many molecules and compartments in the brain with different optical properties renders optical recording and analysis challenging. Of interest is to pinpoint the advantages and constraints of electrophysiological versus optical methods to determine how they can complement each other. For example, optogenetic manipulation of specific cellular subpopulations, while measuring the responses of the neurons using HD-MEAs, will allow for studying functional roles of different classes of neurons (El Hady et al. 2013). Additionally, the effect of different optogenetic therapies to compensate for neuronal dysfunction can be tested with HD-MEAs.

Data obtained from next generation HD-MEAs and multimodal experiments require advanced computational analysis and modeling techniques. Fast implementations of spike-sorting algorithms and parallel computing are needed to handle the large amounts of data produced during long-term HD-MEA experiments. Multiscale modeling, a systems biology technique, may be employed to synchronize events recorded at different time and spatial scales. Overall, all data analysis methods need to be optimized to extract meaningful information within a feasible time from the massive amounts of datasets produced.

References

Alivisatos, A. P., Andrews, A. M., Boyden, E. S., Chun, M., Church, G. M., Deisseroth, K., et al. (2013). Nanotools for neuroscience and brain activity mapping. *ACS Nano, 7*, 1850–1866.

Alpha MED. Scientific Inc. http://www.med64.com

Amin, H., Maccione, A., Marinaro, F., Zordan, S., Nieus, T., & Berdondini, L. (2016). Electrical responses and spontaneous activity of human iPS-derived neuronal networks characterized for 3-month culture with 4096-electrode arrays. *Frontiers in Neuroscience, 10*, 121.

Andersen, R. A., Hwang, E. J., & Mulliken, G. H. (2010). Cognitive neural prosthetics. *Annual Review of Psychology, 61*, 169–90, C1–3.

Angotzi, G. N., Malerba, M., Boi, F., Miele, E., Maccione, A., Amin, H., et al. (2018). A synchronous neural recording platform for multiple high-resolution CMOS probes and passive electrode arrays. *IEEE Transactions on Biomedical Circuits and Systems, 12*(3), 532–542.

Annecchino, L. A., Morris, A. R., Copeland, C. S., Agabi, O. E., Chadderton, P., & Schultz, S. R. (2017). Robotic automation of in vivo two-photon targeted whole-cell patch-clamp electrophysiology. *Neuron, 95*, 1048–1055.e3.

Aziz, J. N. Y., Abdelhalim, K., Shulyzki, R., Genov, R., Bardakjian, B. L., Derchansky, M., et al. (2009). 256-channel neural recording and delta compression microsystem with 3D electrodes. *IEEE Journal of Solid-State Circuits, 44*, 995–1005.

Bakkum, D. J., Chao, Z. C., & Potter, S. M. (2008). Long-term activity-dependent plasticity of action potential propagation delay and amplitude in cortical networks. *PLoS One, 3*, e2088.

Bakkum, D. J., Frey, U., Radivojevic, M., Russell, T. L., Müller, J., Fiscella, M., et al. (2013). Tracking axonal action potential propagation on a high-density microelectrode array across hundreds of sites. *Nature Communications, 4*, 2181.

Ballini, M., Muller, J., Livi, P., Chen, Y., Frey, U., Stettler, A., et al. (2014). A 1024-channel CMOS microelectrode array with 26,400 electrodes for recording and stimulation of electrogenic cells in vitro. *IEEE Journal of Solid-State Circuits, 49*, 2705–2719.

Baumann, W., Lehmann, M., Schwinde, A., Ehret, R., Brischwein, M., & Wolf, B. (1999). Microelectronic sensor system for microphysiological application on living cells. *Sensors and Actuators B: Chemical, 55*, 77–89.

Berdondini, L., Massobrio, P., Chiappalone, M., Tedesco, M., Imfeld, K., Maccione, A., et al. (2009). Extracellular recordings from locally dense microelectrode arrays coupled to dissociated cortical cultures. *Journal of Neuroscience Methods, 177*, 386–396.

Berdondini, L., Overstolz, T., de Rooij, N., Koudelka-Hep, M., Martinoia, S., Seitz, P., et al. (2002). High resolution electrophysiological activity imaging of in-vitro neuronal networks. In *Microtechnologies in Medicine & Biology 2nd Annual International IEEE-EMB Special Topic Conference on* (IEEE) (pp. 241–244). Retrieved February 1, 2011, from http://ieeexplore.ieee.org/xpls/abs_all.jsp?arnumber=1002322

Berényi, A., Somogyvári, Z., Nagy, A. J., Roux, L., Long, J. D., Fujisawa, S., et al. (2014). Large-scale, high-density (up to 512 channels) recording of local circuits in behaving animals. *Journal of Neurophysiology, 111*, 1132–1149.

Bergveld, P. (1970). Development of an ion-sensitive solid-state device for neurophysiological measurements. *IEEE Transactions on Biomedical Engineering, 17*, 70–71.

Bertotti, G., Velychko, D., Dodel, N., Keil, S., Wolansky, D., Tillak, B., et al. (2014). A CMOS-based sensor array for in-vitro neural tissue interfacing with 4225 recording sites and 1024 stimulation sites. In *Biomedical Circuits and Systems Conference (BioCAS) (Lausanne, Switzerland)* (pp. 304–307)

Besl, B., & Fromherz, P. (2002). Transistor array with an organotypic brain slice: Field potential records and synaptic currents. *The European Journal of Neuroscience, 15*, 999–1005.

Blanche, T. J., Spacek, M. A., Hetke, J. F., & Swindale, N. V. (2005). Polytrodes: High-density silicon electrode arrays for large-scale multiunit recording. *Journal of Neurophysiology, 93*, 2987–3000.

Boudes, M., Pieraut, S., Valmier, J., Carroll, P., & Scamps, F. (2008). Single-cell electroporation of adult sensory neurons for gene screening with RNA interference mechanism. *Journal of Neuroscience Methods, 170*, 204–211.

Buzsáki, G., Anastassiou, C. A., & Koch, C. (2012). The origin of extracellular fields and currents—EEG, ECoG, LFP and spikes. *Nature Reviews. Neuroscience, 13*, 407–420.

Camuñas-Mesa, L. A., & Quiroga, R. Q. (2013). A detailed and fast model of extracellular recordings. *Neural Computation, 25*, 1191–1212.

Cheney, P. D., & Fetz, E. E. (1985). Comparable patterns of muscle facilitation evoked by individual corticomotoneuronal (CM) cells and by single intracortical microstimuli in primates: Evidence for functional groups of CM cells. *Journal of Neurophysiology, 53*, 786–804.

Cogan, S. F. (2008). Neural stimulation and recording electrodes. *Annual Review of Biomedical Engineering, 10*, 275–309.

Contreras, D. (2004). Electrophysiological classes of neocortical neurons. *Neural Networks, 17*, 633–646.

Csicsvari, J., Henze, D. a., Jamieson, B., Harris, K. D., Sirota, A., Barthó, P., et al. (2003). Massively parallel recording of unit and local field potentials with silicon-based electrodes. *Journal of Neurophysiology, 90*, 1314–1323.

Cui, X., Lee, V. a., Raphael, Y., Wiler, J. a., Hetke, J. F., Anderson, D. J., et al. (2001). Surface modification of neural recording electrodes with conducting polymer/biomolecule blends. *Journal of Biomedical Materials Research, 56*, 261–272.

DeBusschere, B. D., & Kovacs, G. T. (2001). Portable cell-based biosensor system using integrated CMOS cell-cartridges. *Biosensors & Bioelectronics, 16*, 543–556.

Destexhe, A., Contreras, D., & Steriade, M. (1999). Spatiotemporal analysis of local field potentials and unit discharges in cat cerebral cortex during natural wake and sleep states. *The Journal of Neuroscience, 19*, 4595–4608.

Dipalo, M., Melle, G., Lovato, L., Jacassi, A., Santoro, F., Caprettini, V., et al. (2018). Plasmonic meta-electrodes allow intracellular recordings at network level on high-density CMOS-multi-electrode arrays. *Nature Nanotechnology, 13*, 965.

Doudna, J. A., & Charpentier, E. (2014). The new frontier of genome engineering with CRISPR-Cas9. *Science (80), 346*, 1258096–1258096.

Dragas, J., Viswam, V., Shadmani, A., Chen, Y., Bounik, R., Stettler, A., et al. (2017). In vitro multi-functional microelectrode array featuring 59,760 electrodes, 2048 electrophysiology channels, stimulation, impedance measurement, and neurotransmitter detection channels. *IEEE Journal of Solid-State Circuits, 52*, 1–15.

Du, J., Blanche, T. J., Harrison, R. R., Lester, H. A., & Masmanidis, S. C. (2011). Multiplexed, high density electrophysiology with nanofabricated neural probes. *PLoS One, 6*, e26204.

Eaton, K. P., & Henriquez, C. S. (2005). Confounded spikes generated by synchrony within neural tissue models. *Neurocomputing, 65–66*, 851–857.

Egert, U., Heck, D., & Aertsen, A. (2002). Two-dimensional monitoring of spiking networks in acute brain slices. *Experimental Brain Research, 142*, 268–274.

Eickenscheidt, M., Jenkner, M., Thewes, R., Fromherz, P., & Zeck, G. (2012). Electrical stimulation of retinal neurons in epiretinal and subretinal configuration using a multicapacitor array. *Journal of Neurophysiology, 107*, 2742–2755.

Eilers, J., & Konnerth, A. (2009). Dye loading with patch pipettes. *Cold Spring Harbor Protocols, 2009*, pdb.prot5201.

El Hady, A., Afshar, G., Bröking, K., Schlüter, O. M., Geisel, T., Stühmer, W., et al. (2013). Optogenetic stimulation effectively enhances intrinsically generated network synchrony. *Frontiers in Neural Circuits, 7*, 167.

Engle, S. E., Broderick, H. J., & Drenan, R. M. (2012). Local application of drugs to study nicotinic acetylcholine receptor function in mouse brain slices. *Journal of Visualized Experiments, 68*, e50034.

Eversmann, B., Jenkner, M., Hofmann, F., Paulus, C., Brederlow, R., Holzapfl, B., et al. (2003). A 128×128 cmos biosensor array for extracellular recording of neural activity. *IEEE Journal of Solid-State Circuits, 38*, 2306–2317.

Eversmann, B., Lambacher, A., Gerling, T., Kunze, A., Fromherz, P., & Thewes, R. (2011). A neural tissue interfacing chip for in-vitro applications with 32k recording/stimulation channels on an active area of 2.6mm^2. In *2011 Proceedings of the ESSCIRC* (pp. 211–214). Helsinki: IEEE.

Fejtl, M., Stett, A., Nisch, W., Boven, K. H., & Möller, A. (2006). On micro-electrode array revival: Its development, sophistication of recording, and stimulation. In M. Taketani & M. Baudry (Eds.), *Advances in network electrophysiology* (pp. 24–37). New York: Springer.

Ferrea, E., Maccione, A., Medrihan, L., Nieus, T., Ghezzi, D., Baldelli, P., et al. (2012). Large-scale, high-resolution electrophysiological imaging of field potentials in brain slices with microelectronic multielectrode arrays. *Frontiers in Neural Circuits, 6*, 80.

Fiscella, M., Farrow, K., Jones, I. L., Jäckel, D., Müller, J., Frey, U., et al. (2012). Recording from defined populations of retinal ganglion cells using a high-density CMOS-integrated microelectrode array with real-time switchable electrode selection. *Journal of Neuroscience Methods, 211*, 103–113.

Fiscella, M., Franke, F., Farrow, K., Müller, J., Roska, B., Azeredo da Silveira, R., et al. (2015). Visual coding with a population of direction-selective neurons. *Journal of Neurophysiology, 114*, 2485–2499.

Fiscella, M., Franke, F., Müller, J., Jones, I. L., & Hierlemann, A. (2014). *Decoding of motion directions by direction-selective retina cells*. In Proceedings of the 9th International Meeting on Substrate-Integrated Microelectrode Arrays, Reutlingen, Germany, 98–99.

Franke, F., Fiscella, M., Sevelev, M., Roska, B., Hierlemann, A., & Azeredo da Silveira, R. (2016). Structures of neural correlation and how they favor coding. *Neuron, 89*, 409–422.

Franks, W., Heer, F., McKay, I., Taschini, S., Sunier, R., Hagleitner, C., et al. (2003). CMOS monolithic microelectrode array for stimulation and recording of natural neural networks. in *TRANSDUCERS '03. 12th International Conference on Solid-State Sensors, Actuators and Microsystems. Digest of Technical Papers (Cat. No.03TH8664)* (pp. 963–966). Boston: IEEE.

Franks, W., Schenker, I., Schmutz, P., & Hierlemann, A. (2005). Impedance characterization and modeling of electrodes for biomedical applications. *IEEE Transactions on Biomedical Engineering, 52*, 1295–1302.

Frey, U., Egert, U., Heer, F., Hafizovic, S., & Hierlemann, A. (2009a). Microelectronic system for high-resolution mapping of extracellular electric fields applied to brain slices. *Biosensors & Bioelectronics, 24*, 2191–2198.

Frey, U., Egert, U., Jackel, D., Sedivy, J., Ballini, M., Livi, P., et al. (2009b). Depth recording capabilities of planar high-density microelectrode arrays. in *2009 4th International IEEE/EMBS Conference on Neural Engineering* (pp. 207–210). Antalya: IEEE.

Frey, U., Sedivy, J., Heer, F., Pedron, R., Ballini, M., Mueller, J., et al. (2010). Switch-matrix-based high-density microelectrode array in CMOS technology. *IEEE Journal of Solid-State Circuits, 45*, 467–482.

Fromherz, P., Offenhausser, A., Vetter, T., & Weis, J. (1991). A neuron-silicon junction: A Retzius cell of the leech on an insulated-gate field-effect transistor. *Science (80-), 252*, 1290–1293.

Fujisawa, S., Amarasingham, A., Harrison, M. T., & Buzsáki, G. (2008). Behavior-dependent short-term assembly dynamics in the medial prefrontal cortex. *Nature Neuroscience, 11*, 823–833.

Gandolfo, M., Maccione, a., Tedesco, M., Martinoia, S., & Berdondini, L. (2010). Tracking burst patterns in hippocampal cultures with high-density CMOS-MEAs. *Journal of Neural Engineering, 7*, 56001.

Gesteland, R., Howland, B., Lettvin, J., & Pitts, W. (1959). Comments on microelectrodes. *Proceedings of the IRE, 47*, 1856–1862.

Gong, W., Senčar, J., Bakkum, D. J., Jäckel, D., Obien, M. E. J., Radivojevic, M., et al. (2016). Multiple single-unit long-term tracking on organotypic hippocampal slices using high-density microelectrode arrays. *Frontiers in Neuroscience, 10*, 537.

Gray, C. M., Maldonado, P. E., Wilson, M., & McNaughton, B. (1918). Tetrodes markedly improve the reliability and yield of multiple single-unit isolation from multi-unit recordings in cat striate cortex. *Journal of Neuroscience Methods, 63*, 43–54.

Greschner, M., Field, G. D., Li, P. H., Schiff, M. L., Gauthier, J. L., Ahn, D., et al. (2014). A polyaxonal amacrine cell population in the primate retina. *The Journal of Neuroscience, 34*, 3597–3606.

Greve, F., Lichtenberg, J., Kirstein, K.-U. U., Frey, U., Perriard, J.-C., & Hierlemann, A. (2007). A perforated CMOS microchip for immobilization and activity monitoring of electrogenic cells. *Journal of Micromechanics and Microengineering, 17*, 462–471.

Gross, G., Rieske, E., Kreutzberg, G., & Meyer, A. (1977). A new fixed-array multi-microelectrode system designed for long-term monitoring of extracellular single unit neuronal activity in vitro. *Neuroscience Letters, 6*, 101–105.

Habibey, R., Latifi, S., Mousavi, H., Pesce, M., Arab-Tehrany, E., & Blau, A. (2017). A multielectrode array microchannel platform reveals both transient and slow changes in axonal conduction velocity. *Scientific Reports, 7*, 1–14.

Hafizovic, S., Heer, F., Ugniwenko, T., Frey, U., Blau, A., Ziegler, C., et al. (2007). A CMOS-based microelectrode array for interaction with neuronal cultures. *Journal of Neuroscience Methods, 164*, 93–106.

Hai, A., Dormann, A., Shappir, J., Yitzchaik, S., Bartic, C., Borghs, G., et al. (2009). Spine-shaped gold protrusions improve the adherence and electrical coupling of neurons with the surface of micro-electronic devices. *Journal of The Royal Society Interface, 6*, 1153–1165.

Hai, A., & Spira, M. E. (2012). On-chip electroporation, membrane repair dynamics and transient in-cell recordings by arrays of gold mushroom-shaped microelectrodes. *Lab on a Chip, 12*, 2865–2873.

Harris, K. D., Henze, D. A., Csicsvari, J., Hirase, H., & Buzsáki, G. (2000). Accuracy of tetrode spike separation as determined by simultaneous intracellular and extracellular measurements. *Journal of Neurophysiology, 84,* 401–414.

Harrison, R. R. (2008). The design of integrated circuits to observe brain activity. *Proceedings of the IEEE, 96,* 1203–1216.

Hashimoto, T., Elder, C. M., & Vitek, J. L. (2002). A template subtraction method for stimulus artifact removal in high-frequency deep brain stimulation. *Journal of Neuroscience Methods, 113,* 181–186.

Hassibi, A., Navid, R., Dutton, R. W., & Lee, T. H. (2004). Comprehensive study of noise processes in electrode electrolyte interfaces. *Journal of Applied Physics, 96,* 1074.

Hassler, C., Boretius, T., & Stieglitz, T. (2011). Polymers for neural implants. *Journal of Polymer Science Part B: Polymer Physics, 49,* 18–33.

Heer, F. (2005). *CMOS-based microelectrode array for communication with electrogenic cells.* PhD thesis, No. 16330, Zurich: ETH Zurich.

Heer, F., Franks, W., Blau, A., Taschini, S., Ziegler, C., Hierlemann, A., et al. (2004). CMOS microelectrode array for the monitoring of electrogenic cells. *Biosensors & Bioelectronics, 20,* 358–366.

Heer, F., Hafizovic, S., Franks, W., Blau, A., Ziegler, C., & Hierlemann, A. (2006). CMOS microelectrode array for bidirectional interaction with neuronal networks. *IEEE Journal of Solid-State Circuits, 41,* 1620–1629.

Heer, F., Hafizovic, S., Ugniwenko, T., Frey, U., Franks, W., Perriard, E., et al. (2007). Single-chip microelectronic system to interface with living cells. *Biosensors & Bioelectronics, 22,* 2546–2553.

Henze, D. A., Borhegyi, Z., Csicsvari, J., Mamiya, A., Harris, K. D., & Buzsáki, G. (2000). Intracellular features predicted by extracellular recordings in the hippocampus in vivo. *Journal of Neurophysiology, 84,* 390–400.

Herwik, S., Kisban, S., Aarts, A. A. A., Seidl, K., Girardeau, G., Benchenane, K., et al. (2009). Fabrication technology for silicon-based microprobe arrays used in acute and sub-chronic neural recording. *Journal of Micromechanics and Microengineering, 19,* 74008.

Hierlemann, A., Frey, U., Hafizovic, S., & Heer, F. (2011). Growing cells atop microelectronic chips: Interfacing electrogenic cells in vitro with CMOS-based microelectrode arrays. *Proceedings of the IEEE, 99,* 252–284.

Huang, X.-J., O'Mahony, A. M., & Compton, R. G. (2009). Microelectrode arrays for electrochemistry: Approaches to fabrication. *Small, 5,* 776–788.

Huys, R., Braeken, D., Jans, D., Stassen, A., Collaert, N., Wouters, J., et al. (2012). Single-cell recording and stimulation with a 16 k micro-nail electrode array integrated on a 0.18 μm CMOS chip. *Lab on a Chip, 12,* 1274–1280.

Imfeld, K., Neukom, S., Maccione, A., Bornat, Y., Martinoia, S., Farine, P.-A., et al. (2008). Large-scale, high-resolution data acquisition system for extracellular recording of electrophysiological activity. *IEEE Transactions on Biomedical Engineering, 55,* 2064–2073.

Jäckel, D., Bakkum, D. J., Russell, T. L., Müller, J., Radivojevic, M., Frey, U., et al. (2017). Combination of high-density microelectrode array and patch clamp recordings to enable studies of multisynaptic integration. *Scientific Reports, 7,* 978.

Jäckel, D., Frey, U., Fiscella, M., Franke, F., & Hierlemann, A. (2012). Applicability of independent component analysis on high-density microelectrode array recordings. *Journal of Neurophysiology, 108,* 334–348.

Jenkner, M., Tartagni, M., Hierlemann, A., & Thewes, R. (2004). Cell-based CMOS sensor and actuator arrays. *IEEE Journal of Solid-State Circuits, 39,* 2431–2437.

Jobling, D. T., Smith, J. G., & Wheal, H. V. (1981). Active microelectrode array to record from the mammalian central nervous system in vitro. *Medical & Biological Engineering & Computing, 19,* 553–560.

Jochum, T., Denison, T., & Wolf, P. (2009). Integrated circuit amplifiers for multi-electrode intracortical recording. *Journal of Neural Engineering, 6,* 012001–012026.

Johnson, B., Peace, S. T., Cleland, T. A., & Molnar, A. (2013a). A 50 μm pitch, 1120-channel, 20 kHz frame rate microelectrode array for slice recording. In *2013 IEEE Biomedical Circuits and Systems Conference (BioCAS), Rotterdam* (pp. 109–112).

Johnson, B., Peace, S. T., Wang, A., Cleland, T. A., & Molnar, A. (2013b). A 768-channel CMOS microelectrode array with angle sensitive pixels for neuronal recording. *IEEE Sensors Journal, 13*, 3211–3218.

Jones, I. L., Russell, T. L., Farrow, K., Fiscella, M., Franke, F., Müller, J., et al. (2015). A method for electrophysiological characterization of hamster retinal ganglion cells using a high-density CMOS microelectrode array. *Frontiers in Neuroscience, 9*, 1–16.

Jones, K. E., Campbell, P. K., & Normann, R. a. (1992). A glass/silicon composite intracortical electrode array. *Annals of Biomedical Engineering, 20*, 423–437.

Katzner, S., Nauhaus, I., Benucci, A., Bonin, V., Ringach, D. L., & Carandini, M. (2009). Local origin of field potentials in visual cortex. *Neuron, 61*, 35–41.

Keefer, E. W., Botterman, B. R., Romero, M. I., Rossi, A. F., & Gross, G. W. (2008). Carbon nanotube coating improves neuronal recordings. *Nature Nanotechnology, 3*, 434–439.

Kim, R., Joo, S., Jung, H., Hong, N., & Nam, Y. (2014). Recent trends in microelectrode array technology for in vitro neural interface platform. *Biomedical Engineering Letters, 4*, 129–141.

Kipke, D. R., Vetter, R. J., Williams, J. C., & Hetke, J. F. (2003). Silicon-substrate intracortical microelectrode arrays for long-term recording of neuronal spike activity in cerebral cortex. *IEEE Transactions on Neural Systems and Rehabilitation Engineering, 11*, 151–155.

Kodandaramaiah, S. B., Flores, F., Holst, G., Wickersham, I., Brown, E., Forest, C. R., et al. (2014). The multipatcher: a robot for high density measurement of intracellular recordings in vivo. In *Proceedings of the Biomedical Engineering Society (BMES), San Antonio, TX*.

Kodandaramaiah, S. B., Franzesi, G. T., Chow, B. Y., Boyden, E. S., & Forest, C. R. (2012). Automated whole-cell patch-clamp electrophysiology of neurons in vivo. *Nature Methods, 9*, 585–587.

Koester, P. J., Tautorat, C., Beikirch, H., Gimsa, J., & Baumann, W. (2010). Recording electric potentials from single adherent cells with 3D microelectrode arrays after local electroporation. *Biosensors & Bioelectronics, 26*, 1731–1735.

Lambacher, a., Vitzthum, V., Zeitler, R., Eickenscheidt, M., Eversmann, B., Thewes, R., et al. (2010). Identifying firing mammalian neurons in networks with high-resolution multi-transistor array (MTA). *Applied Physics A: Materials Science & Processing, 102*, 1–11.

Lempka, S. F., Johnson, M. D., Moffitt, M. A., Otto, K. J., Kipke, D. R., & McIntyre, C. C. (2011). Theoretical analysis of intracortical microelectrode recordings. *Journal of Neural Engineering, 8*, 45006.

Lewandowska, M. K., Bakkum, D. J., Rompani, S. B., & Hierlemann, A. (2015). Recording large extracellular spikes in microchannels along many axonal sites from individual neurons. *PLoS One, 10*, e0118514.

Lewandowska, M. K., Radivojević, M., Jäckel, D., Müller, J., & Hierlemann, A. R. (2016). Cortical axons, isolated in channels, display activity-dependent signal modulation as a result of targeted stimulation. *Frontiers in Neuroscience, 10*. https://doi.org/10.3389/fnins.2016.00083

Li, N., Tourovskaia, A., & Folch, A. (2003). Biology on a chip: Microfabrication for studying the behavior of cultured cells. *Critical Reviews in Biomedical Engineering, 31*, 423–488.

Litke, A. M., Bezayiff, N., Chichilnisky, E. J., Cunningham, W., Dabrowski, W., Grillo, A. A., et al. (2004). What does the eye tell the brain?: Development of a system for the large-scale recording of retinal output activity. *IEEE Transactions on Nuclear Science, 51*, 1434–1440.

Liu, X., Demosthenous, A., & Donaldson, N. (2007). On the noise performance of pt. electrodes. *Conference Proceedings: Annual International Conference of the IEEE Engineering in Medicine and Biology Society, 2007*, 434–436.

Livi, P., Heer, F., Frey, U., Bakkum, D. J., & Hierlemann, A. (2010). Compact voltage and current stimulation buffer for high-density microelectrode arrays. *IEEE Transactions on Biomedical Circuits and Systems, 4*, 372–378.

Llinas, R. (1988). The intrinsic electrophysiological properties of mammalian neurons: Insights into central nervous system function. *Science (80-), 242*, 1654–1664.

Lloyd, J. I., Thomas, R., Michele, F., Felix, F., Jan, M., Milos, R., et al. (2014). Characterization of mammalian retinal ganglion cell response to voltage stimulus. In *Proceedings of the ninth International Meeting on Substrate-Integrated Microelectrode Arrays, Reutlingen, Germany* (pp. 74–75).

Lopez, C. M., Andrei, A., Mitra, S., Welkenhuysen, M., Eberle, W., Bartic, C., et al. (2014). An implantable 455-active-electrode 52-channel CMOS neural probe. *IEEE Journal of Solid-State Circuits, 49*, 248–261.

Lopez, C. M., Mitra, S., Putzeys, J., Raducanu, B., Ballini, M., Andrei, A., et al. (2016). 22.7 A 966-electrode neural probe with 384 configurable channels in 0.13 µm SOI CMOS. In *2016 IEEE International Solid-State Circuits Conference (ISSCC)* (pp. 392–393). IEEE.

Lopez, C. M., Chun, H. S., Wang, S., Berti, L., Putzeys, J., Van Den Bulcke, C., et al. (2018, Nov). A multimodal CMOS MEA for high-throughput intracellular action potential measurements and impedance spectroscopy in drug-screening applications. *IEEE Journal of Solid-State Circuits, 53*(11), 3076–3086.

Ludwig, K. A., Uram, J. D., Yang, J., Martin, D. C., & Kipke, D. R. (2006). Chronic neural recordings using silicon microelectrode arrays electrochemically deposited with a poly(3,4-ethylenedioxythiophene) (PEDOT) film. *Journal of Neural Engineering, 3*, 59–70.

Maccione, A., Hennig, M. H., Gandolfo, M., Muthmann, O., van Coppenhagen, J., Eglen, S. J., et al. (2014). Following the ontogeny of retinal waves: Pan-retinal recordings of population dynamics in the neonatal mouse. *The Journal of Physiology, 592*, 1545–1563.

Maccione, A., Simi, A., Nieus, T., Gandolfo, M., Imfeld, K., Ferrea, E., et al. (2013). Sensing and actuating electrophysiological activity on brain tissue and neuronal cultures with a high-density CMOS-MEA. In *2013 Transducers & Eurosensors XXVII: The 17th International Conference on Solid-State Sensors, Actuators and Microsystems (TRANSDUCERS & EUROSENSORS XXVII)* (pp. 752–755). Barcelona: IEEE.

Marblestone, A. H., Zamft, B. M., Maguire, Y. G., Shapiro, M. G., Cybulski, T. R., Glaser, J. I., et al. (2013). Physical principles for scalable neural recording. *Frontiers in Computational Neuroscience, 7*, 137.

Martinez, J., Pedreira, C., Ison, M. J., & Quian Quiroga, R. (2009). Realistic simulation of extracellular recordings. *Journal of Neuroscience Methods, 184*, 285–293.

Medrihan, L., Ferrea, E., Greco, B., Baldelli, P., & Benfenati, F. (2014). Asynchronous GABA release is a key determinant of tonic inhibition and controls neuronal excitability: A study in the synapsin II−/− mouse. *Cerebral Cortex, 25*, 3356–3368.

Menzler, J., & Zeck, G. (2011). Network oscillations in rod-degenerated mouse retinas. *The Journal of Neuroscience, 31*, 2280–2291.

Montgomery, S. M., Sirota, A., & Buzsáki, G. (2008). Theta and gamma coordination of hippocampal networks during waking and rapid eye movement sleep. *The Journal of Neuroscience, 28*, 6731–6741.

Moxon, K. A. (1999). Multichannel electrode design: Considerations for different applications. In M. A. L. Nicolelis (Ed.), *Methods for neural ensemble recordings* (pp. 25–45). Boca Raton: CRC Press.

Müller, J., Bakkum, D. J., & Hierlemann, A. (2013). Sub-millisecond closed-loop feedback stimulation between arbitrary sets of individual neurons. *Frontiers in Neural Circuits, 6*, 1–11.

Müller, J., Ballini, M., Livi, P., Chen, Y., Radivojevic, M., Shadmani, A., et al. (2015). High-resolution CMOS MEA platform to study neurons at subcellular, cellular, and network levels. *Lab on a Chip, 15*, 2767–2780.

Muller, R., Gambini, S., & Rabaey, J. M. (2012). A 0.013 mm2, 5uW, DC-coupled neural signal acquisition IC with 0.5 V supply. *IEEE Journal of Solid-State Circuits, 47*, 232–243.

Multi Channel Systems GmbH. http://www.multichannelsystems.com

Nam, Y., & Wheeler, B. C. (2011). In vitro microelectrode array technology and neural recordings. *Critical Reviews in Biomedical Engineering, 39*, 45–61.

Nelson, M. J., & Pouget, P. (2010). Do electrode properties create a problem in interpreting local field potential recordings? *Journal of Neurophysiology, 103*, 2315–2317.

Nelson, M. J., Pouget, P., Nilsen, E. a., Patten, C. D., & Schall, J. D. (2008). Review of signal distortion through metal microelectrode recording circuits and filters. *Journal of Neuroscience Methods, 169*, 141–157.

Ness, T. V., Chintaluri, C., Potworowski, J., Łęski, S., Głąbska, H., Wójcik, D. K., et al. (2015). Modelling and analysis of electrical potentials recorded in microelectrode arrays (MEAs). *Neuroinformatics*. https://doi.org/10.1007/s12021-015-9265-6

Nevian, T., & Helmchen, F. (2007). Calcium indicator loading of neurons using single-cell electroporation. *Pflügers Archiv-European Journal of Physiology, 454*, 675–688.

Nisch, W., Böck, J., Egert, U., Hämmerle, H., & Mohr, A. (1994). A thin film microelectrode array for monitoring extracellular neuronal activity in vitro. *Biosensors & Bioelectronics, 9*, 737–741.

O'Keefe, J., & Recce, M. L. (1993). Phase relationship between hippocampal place units and the EEG theta rhythm. *Hippocampus, 3*, 317–330.

Obien, M. E. J., Deligkaris, K., Bullmann, T., Bakkum, D. J., & Frey, U. (2015). Revealing neuronal function through microelectrode array recordings. *Frontiers in Neuroscience, 8*. https://doi.org/10.3389/fnins.2014.00423

Obien, M. E. J., Hierlemann, A., & Frey, U. (2014). Technique for analysis of purkinje cell sub-cellular functional dynamics in acute cerebellar slices using a high-density microelectrode array. In *Proceedings of the 9th International Meeting on Substrate-Integrated Microelectrode Arrays, Reutlingen, Germany* (pp. 88–90).

Offenhäusser, A., Sprössler, C., Matsuzawa, M., & Knoll, W. (1997). Field-effect transistor array for monitoring electrical activity from mammalian neurons in culture. *Biosensors & Bioelectronics, 12*, 819–826.

Ogi, J., Kato, Y., Matoba, Y., Yamane, C., Nagahata, K., Nakashima, Y., et al. (2017, Dec). Twenty-four-micrometer-pitch microelectrode array with 6912-channel readout at 12 kHz via highly scalable implementation for high-spatial-resolution mapping of action potentials. *Biointerphases, 12*(5), 05F402.

Oka, H., Shimono, K., Ogawa, R., Sugihara, H., & Taketani, M. (1999). A new planar multi-electrode array for extracellular recording: Application to hippocampal acute slice. *Journal of Neuroscience Methods, 93*, 61–67.

Olsson III, R. H., & Wise, D. K. (2005). A three-dimensional neural recording microsystem with implantable data compression circuitry. *IEEE Journal of Solid-State Circuits, 40*, 2796–2804.

Paik, S.-J., Park, Y., & Cho, D. D. (2003). Roughened polysilicon for low impedance microelectrodes in neural probes. *Journal of Micromechanics and Microengineering, 13*, 373–379.

Parce, J. W., Owicki, J. C., Kercso, K. M., Sigal, G. B., Wada, H. G., Muir, V. C., et al. (1989). Detection of cell-affecting agents with a silicon biosensor. *Science, 246*, 243–247.

Park, J., Aziz, M. K., Gonzalez, S., Jung, D., Chi, T., Li, S., et al. (2017). A CMOS 22 k-pixel single-cell resolution multi-modality real-time cellular sensing array. In *Proceedings of the Custom Integrated Circuits Conference* (pp. 5–8).

Park, T. H., & Shuler, M. L. (2003). Integration of cell culture and microfabrication technology. *Biotechnology Progress, 19*, 243–253.

Pine, J. (1980). Recording action potentials from cultured neurons with extracellular microcircuit electrodes. Journal of Neuroscience Methods 2, 19–31. Retrieved February 1, 2011, from http://linkinghub.elsevier.com/retrieve/pii/0165027080900424

Radivojevic, M., Franke, F., Altermatt, M., Müller, J., Hierlemann, A., & Bakkum, D. J. (2017). Tracking individual action potentials throughout mammalian axonal arbors. *eLife, 6*, 1–23.

Radivojevic, M., Jäckel, D., Altermatt, M., Müller, J., Viswam, V., Hierlemann, A., et al. (2016). Electrical identification and selective microstimulation of neuronal compartments based on features of extracellular action potentials. *Scientific Reports, 6*, 31332.

Regehr, W. G., Pine, J., Cohan, C. S., Mischke, M. D., & Tank, D. W. (1989). Sealing cultured invertebrate neurons to embedded dish electrodes facilitates long-term stimulation and recording. *Journal of Neuroscience Methods, 30*, 91–106.

Reinhard, K., Mutter, M., Fiscella, M., Müller, J., Franke, F., Hierlemann, A., et al. (2014). Novel insights into visual information processing of human retina. In *Proceedings of the 9th International Meeting on Substrate-Integrated Microelectrode Arrays, Reutlingen, Germany* (p. 102).

Robinson, D. A. (1968). The electrical properties of metal microelectrodes. *Proceedings of the IEEE, 56*, 1065–1071.

Robinson, J. T., Jorgolli, M., & Park, H. (2013). Nanowire electrodes for high-density stimulation and measurement of neural circuits. *Frontiers in Neural Circuits, 7*, 1–5.

Sanchez-Bustamante, C. D., Frey, U., Kelm, J. M., Hierlemann, A., & Fussenegger, M. (2008). Modulation of cardiomyocyte electrical properties using regulated bone morphogenetic protein-2 expression. *Tissue Engineering. Part A, 14*, 1969–1988.

Sasaki, T. (2013). The axon as a unique computational unit in neurons. *Neuroscience Research, 75*, 83–88.

Sasaki, T., Matsuki, N., & Ikegaya, Y. (2011). Action-potential modulation during axonal conduction. *Science, 331*, 599–601.

Schubert, R., Trenholm, S., Balint, K., Kosche, G., Cowan, C. S., Mohr, M. A., et al. (2018). Virus stamping for targeted single-cell infection in vitro and in vivo. *Nature Biotechnology, 36*, 81.

Sedivy, J., Frey, U., Heer, F., Hafizovic, S., & Hierlemann, A. (2007). Multi-chip high-density microelectrode system for electrogenic-cell recording and stimulation. In *2007 IEEE sensors* (pp. 716–719). Atlanta: IEEE.

Segev, R., Goodhouse, J., Puchalla, J., & Berry, M. J. (2004). Recording spikes from a large fraction of the ganglion cells in a retinal patch. *Nature Neuroscience, 7*, 1154–1161.

Seidl, K., Herwik, S., Torfs, T., Neves, H. P., Paul, O., & Ruther, P. (2011). CMOS-based high-density silicon microprobe arrays for electronic depth control in intracortical neural recording. *Journal of Microelectromechanical Systems, 20*, 1439–1448.

Shahrokhi, F., Abdelhalim, K., & Genov, R. (2009). 128-channel fully differential digital neural recording and stimulation interface. In *2009 IEEE International Symposium on Circuits and Systems (IEEE)* (pp. 1249–1252).

Spira, M. E., & Hai, A. (2013). Multi-electrode array technologies for neuroscience and cardiology. *Nature Nanotechnology, 8*, 83–94.

Stett, A., Egert, U., Guenther, E., Hofmann, F., Meyer, T., Nisch, W., et al. (2003). Biological application of microelectrode arrays in drug discovery and basic research. *Analytical and Bioanalytical Chemistry, 377*, 486–495.

Steyaert, M. S. J., & Sansen, W. M. C. (1987). A micropower low-noise monolithic instrumentation amplifier for medical purposes. *IEEE Journal of Solid-State Circuits, 22*, 1163–1168.

Stutzki, H., Leibig, C., Andreadaki, A., Fischer, D., & Zeck, G. (2014). Inflammatory stimulation preserves physiological properties of retinal ganglion cells after optic nerve injury. *Frontiers in Cellular Neuroscience, 8*, 38.

Suk, H.-J., van Welie, I., Kodandaramaiah, S. B., Allen, B., Forest, C. R., & Boyden, E. S. (2017). Closed-loop real-time imaging enables fully automated cell-targeted patch-clamp neural recording in vivo. *Neuron, 95*, 1037–1047.e11.

Tanaka, M., Yanagawa, Y., & Hirashima, N. (2009). Transfer of small interfering RNA by single-cell electroporation in cerebellar cell cultures. *Journal of Neuroscience Methods, 178*, 80–86.

Thomas, C. A., Springer, P. A., Loeb, G. E., Berwald-Netter, Y., & Okum, L. M. (1972). A miniature microelectrode array to monitor the bioelectric activity of cultured cells. *Experimental Cell Research, 74*, 61–66.

Tokuda, T., Yamamoto, A., Kagawa, K., Nunoshita, M., & Ohta, J. (2006). A CMOS image sensor with optical and potential dual imaging function for on-chip bioscientific applications. *Sensors and Actuators A: Physical, 125*, 273–280.

Tsai, D., Sawyer, D., Bradd, A., Yuste, R., & Shepard, K. L. (2017). A very large-scale microelectrode array for cellular-resolution electrophysiology. *Nature Communications, 8*. https://doi.org/10.1038/s41467-017-02009-x

Velychko, D., Eickenscheidt, M., Thewes, R., & Zeck, G. (2014). Simultaneous stimulation and recording of retinal action potentials using capacitively coupled high- density CMOS-based MEAs. In *Proceedings of the 9th International Meeting on Substrate-Integrated Microelectrode Arrays, Reutlingen, Germany* (pp. 78–79).

Viswam, V., Dragas, J., Shadmani, A., Chen, Y., Stettler, A., Mueller, J., et al. (2016). Multi-functional microelectrode array system featuring 59,760 electrodes, 2048 electrophysiology channels, impedance and neurotransmitter measurement units. In *2016 IEEE International Solid-State Circuits Conference, ISSCC 2016, San Francisco, CA, USA, January 31–February 4, 2016* (pp. 394–396).

Viswam, V., Jäckel, D., Ballini, M., Müller, J., Radivojevic, M., Frey, U., et al. (2014). An automated method for characterizing electrode properties of high-density microelectrode arrays. In *Proceedings of the 9th International Meeting on Substrate-Integrated Microelectrode Arrays, Reutlingen, Germany* (pp. 302–303).

Wagenaar, D. A., & Potter, S. M. (2002). Real-time multi-channel stimulus artifact suppression by local curve fitting. *Journal of Neuroscience Methods, 120*, 113–120.

Ward, M. P., Rajdev, P., Ellison, C., & Irazoqui, P. P. (2009). Toward a comparison of microelectrodes for acute and chronic recordings. *Brain Research, 1282*, 183–200.

Weale, R. A. (1951). A new micro-electrode for electro-physiological work. *Nature, 167*, 529–530.

Weis, R., & Fromherz, P. (1997). Frequency dependent signal transfer in neuron transistors. *Physical Review E, 55*, 877–889.

Wise, K. D., Angell, J. B., & Starr, A. (1970). An integrated-circuit approach to extracellular microelectrodes. *IEEE Transactions on Biomedical Engineering, 3*, 238–247.

Wood, C., Williams, C., & Waldron, G. J. (2004). Patch clamping by numbers. *Drug Discovery Today, 9*, 434–441.

Yonehara, K., Fiscella, M., Drinnenberg, A., Esposti, F., Trenholm, S., Krol, J., et al. (2016). Congenital nystagmus gene FRMD7 is necessary for establishing a neuronal circuit asymmetry for direction selectivity. *Neuron, 89*, 177–193.

Yuan, X., Kim, S., Juyon, J., Urbino, M. D., Bullmann, T., Chen, Y., et al. (2016). A microelectrode array with 8,640 electrodes enabling simultaneous full-frame readout at 6.5 kfps and 112-channel switch-matrix readout at 20 kS/s. In *Symposium on VLSI Circuits Digest of Technical Papers, Honolulu, Hawaii* (pp. 258–259).

Yuan, X., Emmenegger, V., Obien, M. E. J., Hierlemann, A., & Frey, U. (2018). Dual-mode microelectrode array featuring 20k electrodes and high SNR for extracellular recording of neural networks. In *2018 IEEE Biomedical Circuits and Systems Conference (BioCAS)* (pp. 1–4).

Zeck, G., Lambacher, A., & Fromherz, P. (2011). Axonal transmission in the retina introduces a small dispersion of relative timing in the ganglion cell population response. *PLoS One, 6*, e20810.